CHALMERS
UNIVERSITY OF TECHNOLOGY

Effect of Al addition on oxidation behavior of Nb-based refractory alloys at elevated temperatures

Master's thesis in Materials Engineering

YUFEI ZHAO

DEPARTMENT OF INDUSTRIAL AND MATERIALS SCIENCE
CHALMERS UNIVERSITY OF TECHNOLOGY

Gothenburg, Sweden 2024
www.chalmers.se

Master's Thesis 2024

Effect of Al addition on oxidation behavior of Nb-based refractory alloys at elevated temperatures

YUFEI ZHAO

CHALMERS
UNIVERSITY OF TECHNOLOGY

Department of Industrial and Materials Science
Chalmers University of Technology
Gothenburg, Sweden 2024

Effect of Al addition on oxidation behavior of Nb-based refractory alloys at elevated temperatures
YUFEI ZHAO

Supervisor: Xiaolong Li, Department of Industrial and Materials Science
Examiner: Sheng Guo, Department of Industrial and Materials Science

Master's Thesis 2024
Department of Industrial and Materials Science
Chalmers University of Technology
SE-412 58 Gothenburg
Sweden
Telephone +46 31 772 1000

Typeset in Microsoft Word
Gothenburg, Sweden 2024

Effect of Al addition on oxidation behavior of Nb-based refractory alloys at elevated temperatures

YUFEI ZHAO
Department of Industrial and Materials Science
Chalmers University of Technology

Abstract

Improving gas turbine efficiency is closely linked to reducing global carbon emissions, which requires the development of materials that can operate at ultra-high temperatures. In this thesis, the oxidation behavior of three quaternary Nb-based refractory alloys, Nb-15Hf-5.5W-4Al, Nb-15Hf-5.5W-8Al, Nb-15Hf-5.5W-12Al (nominal compositions, in at.%) is reported. The alloys were produced by vacuum arc melting, and the oxidation studies were performed at 800℃, 1000℃, and 1200℃ for 1h, 8h, and 24h, respectively, while the phase constitution, microstructure, and composition of oxidation products were analyzed by XRD, SEM, and EDS. Microstructures of three alloys all showed a single-phase bcc structure with a typical dendritic structure, and their Vicker hardness monotonously increased with the increasing Al content. The oxidation products contained different complex oxides including Nb_2O_5, $Hf_6Nb_2O_{17}$, $AlNbO_4$, WO_3, and $Nb_{11}AlO_{29}$. At 800℃, the oxidation behavior was linear, but at higher temperatures, the oxidation behavior was more parabolic. Although oxide layers and transition layers were seen to form in samples after oxidation at 1000℃ and 1200℃, all formed oxide layers were not protective, and consequently, pesting was observed almost in all cases, except the condition of oxidation at 800℃ for 1h. The results showed that adding Al up to 12 at.% helped to improve the oxidation resistance of these Nb-based refractory alloys, but the improvement was still limited and importantly it was not capable of forming a dense and protective oxide layer yet.

Keywords: Refractory alloys, Nb-based alloys, Oxidation resistance, Pesting, Microstructure.

Acknowledgments

I would like to express my deepest gratitude to my supervisor, Xiaolong Li, for his guidance, support, and encouragement throughout this project. Without his help, this thesis could not have been completed successfully, and I am truly thankful for his patience and dedication.

My heartfelt thanks to my examiner Sheng Guo for his support and valuable feedback on this whole project.

I would also like to extend my appreciation to the faculty members and colleagues at the Department of Industrial and Materials Science of Chalmers University of Technology, for their constructive comments and discussions that helped broaden my research perspective. Special thanks to Antonio Mulone for his assistance in my lab skills learning and technical support during my experiments.

I would also like to thank my friends and classmates for their emotional support, feedback, and participation in my defense, which have enriched my academic journey.

Finally, I wish to express my love and appreciation to my family for their unwavering support, understanding, and encouragement throughout this 2-year degree. Their belief in me has been my greatest source of strength.

Thank you all.

Gothenburg, October 2024
Yufei Zhao

Contents

1 Introduction **7**

2 Refractory alloys **9**

2.1 Traditional refractory alloys 9

2.2 Refractory high entropy alloys (RHEAs) 10

3 High-temperature oxidation **17**

3.1 Thermodynamics of oxidation 17

3.2 Kinetics of oxidation 20

3.2.1 Pilling-Bedworth ratio and growth stress 21

3.2.2 Coefficient of thermal expansion (CTE) and thermal stress 22

3.2.3 Linear, parabolic, and logarithmic laws 23

4 Oxidation of refractory alloys **27**

4.1 Conventional protective scales 27

4.2 Pesting 32

4.3 Complex protective scales 33

5 Experimental methods **37**

5.1 Sample preparation 37

5.2 Oxidation studies 37

5.3 Scanning electron microscopy 38

5.4 X-ray diffraction 40

5.5 Hardness test 41

6 Results and discussion **43**

6.1 Pre-oxidation: microstructure, hardness, and phase 43

6.2 Post-oxidation 47

6.2.1 Oxidation kinetics 47

6.2.2 Microstructure and phase constitution of oxidation products 50

7 Conclusions **53**

References **55**

1 Introduction

Global carbon emissions are growing. Improving gas turbine efficiency is important for global natural energy conservation and emission reduction, contributing to a more energy-efficient, low-carbon society. As hotter engines lead to better efficiency, the rise of the working temperature of engine materials has always been an important research topic[1]. However, the operating temperature of an engine is limited by the performance of the engine material, especially in the hottest components, e.g., gas turbine blades. After nearly 80 years of gradual development, turbine blades are mainly made from state-of-the-art nickel-based superalloys. However, even nickel-based superalloys cannot operate at temperatures higher than 1150℃ with their melting points below 1455℃ [2]. Practically, the effective operating temperature of the turbine blades can be increased through an auxiliary cooling system, at unfortunately the cost of reduced thermal efficiency. The thermal efficiency of the current turbine engines would be increased by 50% if turbine engines could work at 1300℃ without auxiliary cooling [3]. Therefore, to overcome this temperature limitation then to release the sacrificed efficiency of gas turbines due to auxiliary cooling, it is necessary to develop new ultra-high temperature materials. Given the demanding performance requirements of engine materials, such as strength at high temperatures (HT), ductility at room temperatures (RT), oxidation resistance along the whole using temperature range, refractory metal and alloys with metallic bonds stand out in the material selection process because of their high melting point, high strength, and reasonable ductility [4], compared with other candidate materials such as intermetallics and ceramics with covalent bonds.

Although refractory metals and alloys possess the potential to be the next generation ultra-high temperature materials, the widely existing trade-off among material performances remains a formidable challenge. Usually, the factors favoring one aspect of the performance tend to adversely affect the others. Ductility and oxidation resistance, for example, will be at the expense when the high strength at HT is sought after [5], [6]. Oxidation resistance is equally important as high strength at HT and ductility at RT, but generally, it receives less attention compared to the other two material performances. This gap motivates the topic of this master thesis.

It is known that the formation of compact and continuously protective oxide scales, such as Al_2O_3, Cr_2O_3, and SiO_2, is effective in preventing the degradation and premature failure of materials under HT [7]. Among them, Al_2O_3 is often considered the best option as it can be thermodynamically stabilized up to 1400 ℃ without volatility. The introduction of aluminum on the other hand can lead to embrittlement and potential loss of strength at HT, and therefore when considering aluminum alloying it is necessary to maintain the balance of material performances [8], [9]. This thesis aims to study the effect of aluminum addition on the oxidation behavior of several carefully designed refractory alloys with a reasonable balance of HT strength and RT ductility, at elevated temperatures.

The objective of this thesis is to conduct high-temperature oxidation experiments on Nb-15Hf-5.5W-4Al, Nb-15Hf-5.5W-8Al, Nb-15Hf-5.5W-12Al Nb-based refractory alloys (nominal compositions, in at.%), at 800℃, 1000℃, and 1200℃ for 1h, 8h, and 24h, respectively. Phase constitution, microstructure and composition of oxidation products under different oxidation conditions will be investigated using techniques including X-ray diffraction (XRD), scanning electron microscopy (SEM), and energy-dispersive X-ray spectroscopy (EDS), to promote a body of knowledge around alloy design and oxidation behavior of refractory alloys and to gain a deeper understanding of their properties at ultra-high temperatures.

2 Refractory alloys

In this chapter, the state-of-the-art of refractory alloys, including traditional refractory alloys and refractory high entropy alloys (RHEAs), will be summarized as follows.

2.1 Traditional refractory alloys

Traditional refractory alloys are mainly composed of tungsten (W), molybdenum (Mo), tantalum (Ta), and niobium (Nb) with other high melting point metals. Refractory alloys are widely used in high-temperature environments, such as aerospace and nuclear energy, due to their excellent mechanical strength and creep resistance at elevated temperatures [10], [11]. Figure 1 (a) shows changes in the tensile strength of several typical refractory metals (Rh, Ta, W, Mo and Nb) at different test temperatures. The high-temperature strength of these metals decreases with increasing temperature. Among them, Re has the highest tensile strength at high temperatures, and even if the temperature exceeds 1500℃, its strength remains at a high level. Ta and W exhibit relatively high tensile strength below 1000℃, but their strength gradually decreases as the temperature rises. The tensile strength of Mo also decreases with increasing temperature, and it decreases significantly at 800℃. Nb exhibits relatively low tensile strength over the entire temperature range, especially at levels above 1000℃ where its strength decreases significantly. Figure 1 (b) compares yield stress between some refractory metals and alloys and state-of-the-art Ni-based superalloys. Although the yield stresses of refractory alloys are in general lower than those of Ni-based superalloys, the retainability of their stress can go to much higher temperatures (1200 ℃) than superalloys. Noticeably, these refractory alloys possess compatible tensile ductility at RT. Some commonly used refractory alloys include but are not limited to C-103, WC-3009, and TZM.

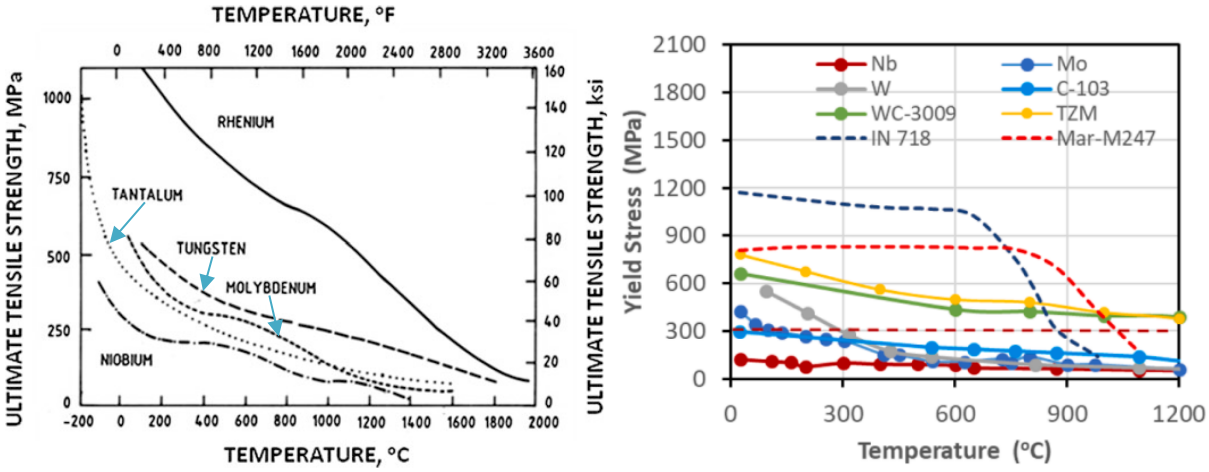

(a) (b)

Figure 1. (a) Tensile strength of refractory metals versus test temperatures [10] (b) Temperature dependence of yield stress for refractory metals and alloys, benchmarked with Ni-based superalloys [11]

Among refractory metals and alloys, Nb and Mo with their alloys are most developed due to their high melting points of 2468℃ and 2617℃, comparable densities of 8.75 and 10.2 g/cm^3, and low DBTT (ductile-to-brittle transition temperature) < -126 ℃ and 27 ℃, respectively. Mechanical properties of several commercial Nb and Mo alloys are listed below in Figure 2 [10]. Mo-based alloys have an even higher stress than Nb-based alloys and can be used at even higher temperatures.

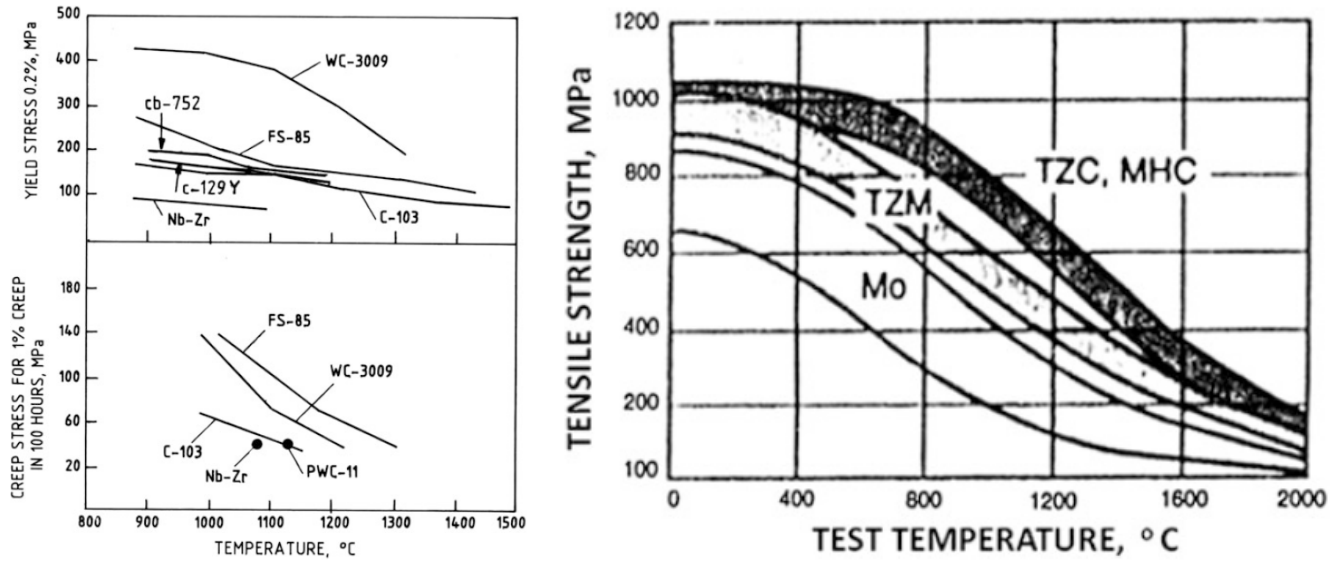

(a) (b)

Figure 2. Elevated-temperature properties of some commercial (a) Nb-based alloys (b) Mo-based alloys[10]

Although these refractory alloys have excellent high-temperature properties, their applications are rather limited [12], [13]. Firstly, they are difficult to manufacture and process, especially Mo and W alloys, which are typically brittle at RT. Secondly, these alloys are highly sensitive to impurities such as oxygen, nitrogen and carbon, and must be processed and used in a strictly controlled environment. In addition, the high density of these materials is not conducive to application in areas that require lightweight materials. To overcome these problems, efforts are required to adjust the alloy compositions, develop new manufacturing techniques, and adopt surface treatment techniques, in order to improve the overall properties and application range of these materials. For example, mechanical alloying and dispersion strengthening can significantly improve their high-temperature strength and oxidation resistance, thus expanding their application prospects [14].

2.2 Refractory high entropy alloys (RHEAs)

Refractory high entropy alloys (RHEAs), as a sub-category of high entropy alloys (HEAs), have attracted great attention in recent years [15] due to their excellent high-temperature properties. Research on HEAs began in 1996 and the first papers on HEAs were published in 2004 by Yeh [16] and Cantor [17]. By mixing multiple elements in nearly equal proportions, HEAs could achieve high strength, excellent wear resistance, good corrosion resistance, and possibly unique magnetic or thermal properties depending on the alloy compositions. The initial motivation for HEAs research was to explore the central region of the phase space of multicomponent alloys [17] and the primary assumption was that high configurational entropy might favor the formation of a single solid solution (SS) phase over multiple phases or intermetallic (IM) phases.

[18]. In general, HEA research prioritizes the quest for a single solid solution phase. Early definitions of HEAs focused on the compositions of five or more principal elements, each in concentrations ranging between 5 and 35 at.% [19]. This definition allows for non-equimolar compositions and permits the inclusion of a small number of minor elements to modify the properties of the alloys, thus expanding the scope of HEAs. Another definition based on the magnitude of the configuration entropy divides the alloys into low ($S^{ss,\ ideal}$ (total configurational molar entropy in an ideal SS, and R is the gas constant) <0.69R), medium (0.69R<$S^{ss,\ ideal}$ <1.61R), and high entropy ($S^{ss,\ ideal}$>1.61R) ranges [19]. Figure 3 shows empirical correlations between atomic radius differences (δ) and mixing enthalpy (ΔH_{mix}) for differentiating phase regions (SS, IM, and AM (amorphous phase)). The diagram has several regions. (SS): The blue region represents solid solutions, usually formed at low atomic radius differences and mixing enthalpy values; (AM): The red region is the amorphous phase, which usually occurs at high δ and highly negative mixing enthalpy values; (IM): The green area indicates the coexistence zone between the solid solution and the intermetallic compounds, which form in the intermediate δ and ΔH_{mix} ranges, or between the intermetallic compounds and the amorphous phase. This empirical diagram can effectively predict the trend of forming different phases in the alloy system.

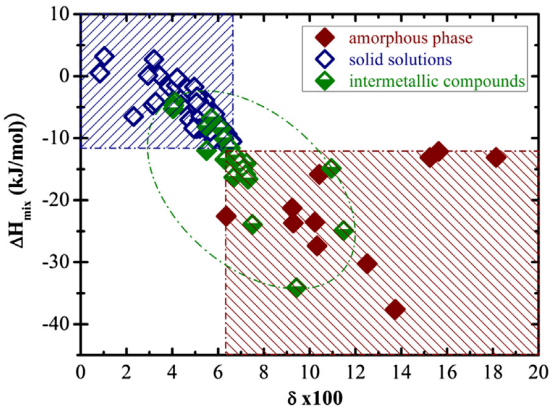

Figure 3: Empirical correlations using δ vs. ΔH_{mix} to distinguish solid solutions (SS), intermetallic phases (IM), and the amorphous phase (AM) regions [20]

As part of the broader concept of HEAs, RHEAs represent a class of HEAs mainly composed of refractory elements, including Group IV (Ti, Zr, Hf), Group V (V, Nb, Ta), and Group VI (Cr, Mo, W) elements. Sometimes non-refractory metals such as Al, Si, Co, or Ni are added for the balance of alloy properties [15]. RHEAs exhibit high strength and heat resistance at high temperatures up to 1600℃, beyond the capacity of traditional high-temperature alloys [4], [21], showing great potential in applications such as the aerospace, energy, nuclear technology, and defense sectors. In 2010, RHEAs were first introduced, which consisted of five refractory elements (Mo, Nb, Ta, V, and W) [4]. In recent years, the research on RHEAs has been growing, with a focus mainly on addressing the need for high-temperature structural materials. The increase in the number of publications on the topic of RHEAs follows an exponential growth pattern, as shown in Figure 4 [22].

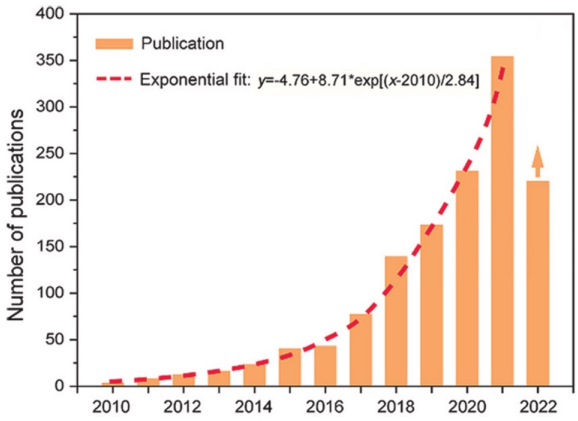

Figure 4: Number of publications on RHEA over the years [22]

The composition of RHEAs is critical to determine their final microstructure and properties [23]. Unlike traditional refractory alloys, RHEAs have a wide range of compositional variations, offering various possibilities for tailoring their properties [24]. Exploration of the compositions of RHEAs is critical to the discovery of new materials with enhanced properties [25]. To achieve that purpose, in recent years researchers have been doing abundant experimental studies and theoretical work using for example high-throughput simulations [26], [27], [28], [29].

Reported RHEAs mainly present a disordered bcc structure, sometimes accompanied by secondary phases such as the Laves phase, B2 phase, hcp phase and other phases like M_5Si_3. The Laves phase enhances high-temperature strength and oxidation resistance but reduces the room-temperature toughness. The ordered B2 phase, sometimes observed as a matrix phase in multiphase RHEAs, provides thermal stability and high-temperature strength retention. The presence of nanometer-sized bcc precipitates in the B2 matrix exhibits unique mechanical properties, similar to that in Ni-based superalloys [21]. Additionally, the addition of small atoms including B, C, and N has been explored to enhance the performance of RHEAs. For example, the addition of B and its segregation at the grain boundaries effectively solves the RT embrittlement issue of some RHEAs, changing the fracture mode from inter-granular to trans-granular [30]. Similarly, C-alloyed RHEAs have been reported to form a single bcc solid solution structure, which altered mechanical and thermal properties [31]. Figure 5 shows the types and quantities of phases that occur in RHEAs with different numbers of phases. The bcc phase is the most common single-phase structure; it occurs the most often, and it is also dominant in biphase alloys. Other phases such as Laves phase, B2 phase, M_5Si_3 usually occur in biphase, three-phase, or even four-phase structures, are far less numerous than the bcc phase.

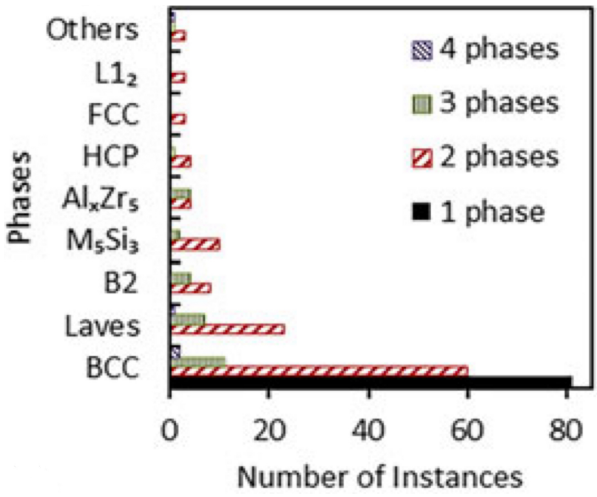

Figure 5. Number of occurrences of different phases in 1-, 2-, 3-, and 4-phase RHEAs [21]

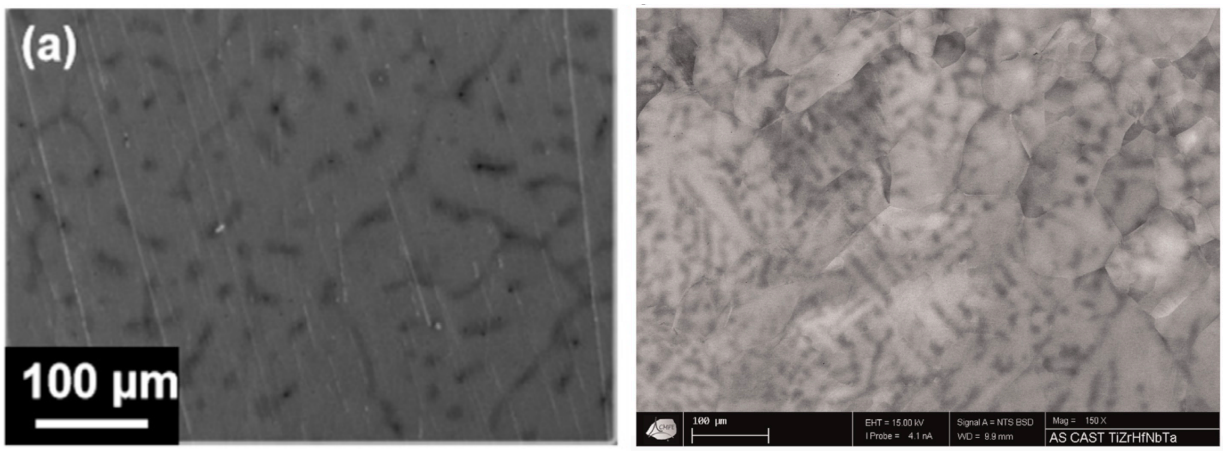

(a) (b)

Figure 6. SEM images of arc-melted (a) VNbMoTaW [21] and (b) TiZrHfNbTa. Dark zones correspond to the presence of micro-segregation at inter-dendritic regions [33]

The microstructure of cast RHEAs often shows a typical dendritic structure, as exemplified in Figure 6 (a) and (b), SEM images of two equi-atomic RHEAs, VNbMoTaW and TiZrHfNbTa. Generally, the elements with high melting points segregate to dendrites and those with low melting points segregate to inter-dendrites.

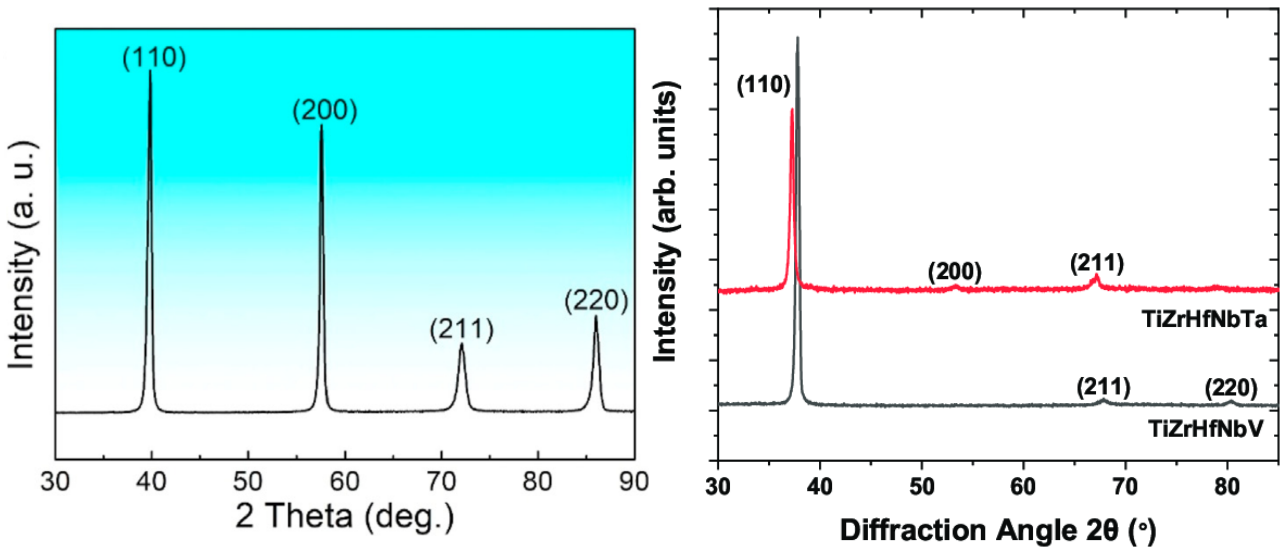

(a) (b)

Figure 7. XRD pattern of arc-melted (a) VNbMoTaW alloy[32] and (b) TiZrHfNbTa and TiZrHfNbV RHEAs. Peaks corresponding to the crystallographic planes of the bcc phase are indicated [34]

XRD analysis is usually used to determine crystal structure and lattice constants. From Figure 7, it is clear that the alloy VNbMoTaW has a first peak of (110), then a second (200), and a third (211), while alloys TiZrHfNbTa and TiZrHfNbV show the second peak as (211) and the third (200). The peak density for (200) is too low, possibly due to texture. Comparing the XRD patterns of TiZrHfNbTa and TiZrHfNbV, the peaks of TiZrHfNbV shift to the right (higher diffraction angle). From Bragg's law:

$$n\lambda = 2dsin\theta$$

when θ gets bigger, d gets smaller, indicating a decrease in the lattice parameters of the crystal structure, mainly due to the much smaller atomic radius of V to that of Ta.

Mechanical properties of RHEAs are usually characteristic of high strength at very high temperatures and brittleness at lower temperatures. Through thermal treatment and thermo-mechanical processing, a better balance of strength and ductility could be achieved, improving the overall mechanical performance of RHEAs and making them more suitable for practical applications. The ultimate goal of the research on RHEAs via optimizing their compositions is to improve their low-temperature ductility without affecting much on high-temperature strength. Notably, the reported microstructure in as-cast RHEAs may not always represent equilibrium phases. Kinetic restrictions during cooling may freeze high-temperature stable phases, leading to the formation of non-equilibrium microstructures. Thermomechanical processing, including cold deformation and annealing, could induce phase transformations, forming thermodynamically kinetically stable microstructures and hence leading to different mechanical properties to those seen in as-case RHEAs. Figure 8 (a) shows σ_y (MPa) as a function of temperature (K) for different RHEAs, also known as RCCAs (refractory complex concentrated alloys). RCCAs like $AlMo_{0.5}NbTa_{0.5}TiZr$ and CrNbTiZr have relatively high yield strength at high temperatures, maintaining strength above 1000 MPa up to 1400K. Figure 8 (b) shows σ_y/ρ (MPa-cm^3/g) as a function of temperature (K) for different RCCAs. $AlMo_{0.5}NbTa_{0.5}TiZ$ exhibits high strength/density ratios over a wide temperature range, even exceeding INCONEL 718 and MAR-M 247 at high temperatures. The dashed lines represent typical application requirements: discs, blades, and

thermal protection systems (TPS), showing that some RCCAs are expected to meet or exceed these performance standards in these application areas.

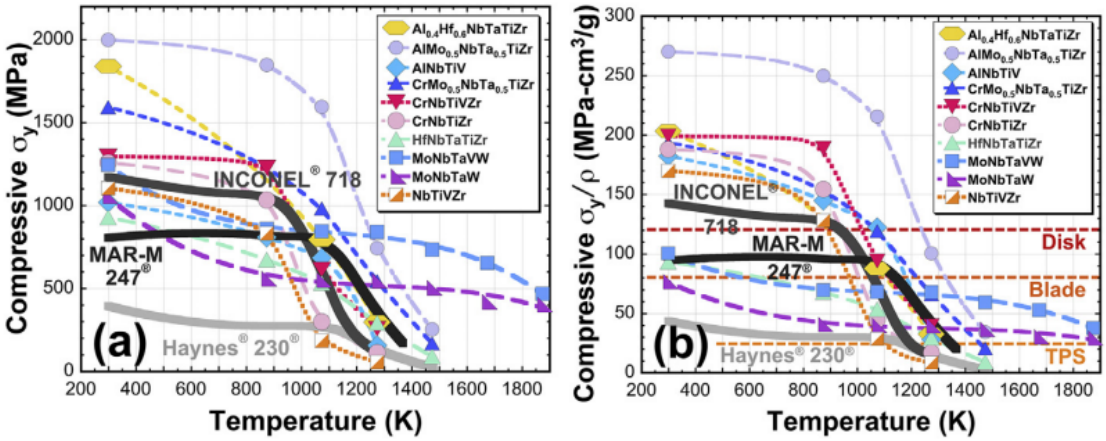

Figure 8: Temperature dependence of (a) compressive yield strength, σ_y, and (b) σ_y normalized by alloy density, ρ, of refractory complex concentrated alloys (RCCAs) [15]

3 High-temperature oxidation

This chapter focuses on the basic theory of oxidation for metals and alloys at elevated temperatures. The term "high temperature" is defined in this context to be 500℃ and above [35]. When designing alloys for high-temperature applications, it is necessary to understand the thermodynamics and kinetics of high-temperature oxidation for predicting material behavior and developing effective protective measures to minimize material degradation. Factors such as alloy composition, temperature, and gas condition affect the formation of oxidation products, and theoretical prediction and experimental investigations are needed. A protective oxide layer that has a non-porous structure and is attached to the metal substrate is essential to ensure the long-term integrity of the material at high temperatures.

3.1 Thermodynamics of oxidation

Thermodynamics studies the behavior of energy and its transformations during various processes. A thermodynamic process describes a thermodynamic system transiting from an initial to a final state. Besides heat and work, thermodynamics includes energies such as kinetic energy, potential energy, internal energy, Gibbs free energy, Helmholtz free energy, etc. This sub-chapter explores the fundamentals of thermodynamics and an important diagram regarding the oxidation of alloys. The core of high-temperature oxidation of alloys is to evaluate whether certain components can react with oxygen in the air. The thermodynamics analysis can be used to predict possible reaction products. The Ellingham diagram which presents the relationship between the standard free energy of formation and temperature will also be explained.

The first law of thermodynamics, known as the principle of conservation of energy, states that in a closed system, the change in internal energy (dU) is equal to the heat added (δQ) to the system plus the work done (δW) on the system. $\delta Q+\delta W=dU$. However, in a closed system where there are changes in potential and/or kinetic energies, the equation becomes $\delta Q+\delta W=dU+dE_p+dE_k$, where d is the differential of a state function, δ is the differential of a path-dependent function, Q is heat, W is work, U is internal energy, E_p is potential energy, and E_k is kinetic energy. The second law of thermodynamics states that heat is never transferred spontaneously from a cold body to a hot body, but only from a hot body to a cold body. The second law determines whether a reaction can proceed, typically under conditions of constant temperature and pressure. The most convenient expression regarding a system's Gibbs free energy (G) can be written as [36]:

$$G = H - TS$$

Enthalpy, H, and entropy, S, are basic thermodynamic parameters for the analysis of high-temperature oxidation reactions. H is a thermodynamic quantity equivalent to the total heat content of a system. It is equal to the internal energy of the system (U) plus the product of pressure (P) and volume (V): $H = U + PV$. S measures the degree of randomness or disorder in a system's atomic or molecular structure, reflecting

the process's irreversibility. An increase in entropy corresponds to an increase in internal chaos and a decrease in the system's internal energy [36]. Under these conditions, the change in free energy (ΔG) of a process according to the second law holds the following implications: ΔG<0 indicates an expected spontaneous reaction, ΔG=0 signifies equilibrium, and ΔG>0 indicates a thermodynamically impossible process.

Thermodynamic equilibrium refers to a state in a single system that shows no macroscopic change in its internal state, or multiple systems exhibit no macroscopic net flow of matter or energy between them. The stability of the reaction products can be predicted by analyzing the possible equilibrium states of the alloy and oxygen under the condition of high-temperature oxidation and the factors affecting these equilibrium states [35]. The chemical potential of a species represents the amount of energy that can be exchanged when the particle number of that species changes, such as during a chemical reaction or phase transition. In a mixture, the chemical potential of a species or component is defined as the partial derivative of the free energy of a thermodynamic system concerning the number of atoms or molecules of that species, keeping other variables (such as temperature, pressure, and the number of other species) constant. The minimum Gibbs free energy determines the system's equilibrium state at constant temperature and pressure.

An Ellingham diagram is a graph showing the standard Gibbs free energy change ($\Delta G°$) for each oxidation reaction as a function of temperature T. All values of $\Delta G°$ are expressed as kJ mol^{-1} O_2. It shows the temperature dependence of the stability of compounds, and the lower the position of the line, the more stable the oxide [35]. The intersection point of the oblique line indicates that the free energy of the reduction of two metal oxides is the same at a specific temperature. In general, negative ΔG values indicate spontaneous reactions, while the position and intersection of the Gibbs free energy curves help predict the reduction behavior of metal oxides at different temperatures. A reaction can be written as:

$$M(s) + O_2(g) = MO_2(s).$$

Then the standard free energy of the reaction can be expressed as:

$$\Delta G° = -RTln(\frac{a_{MO_2}}{a_M P_{O_2}})_{eq}$$

$$P_{O_2}{}^{eq} = \frac{a_{MO_2}}{a_M} exp\frac{\Delta G}{RT} = \frac{a_{MO_2}}{a_M} P_{O_2}{}^{\frac{M}{MO_2}}$$

$P_{O_2}{}^{\frac{M}{MO_2}}$ is the oxygen partial pressure when the metal and oxide coexist. The value of $P_{O_2}{}^{\frac{M}{MO_2}}$ can also be solved by drawing lines on the diagram and finding the intersection point. For example, in Figure 9 [37], the blue line is the free-energy line at the desired experiment temperature of 1000℃, and the red point on the scale bar of P_{O_2} indicates the value of $P_{O_2}{}^{\frac{Ti}{TiO_2}}$. Similarly, drawing a similar line from the point marked H to the scale bar of the H_2/H_2O ratio will obtain the pressure ratio H_2/H_2O for equilibrium between the given metal and oxide, and drawing a line from the point marked C to the CO/CO_2 ratio scale bar will obtain the pressure ratio CO/CO_2.

Refractory metal oxides and Al_2O_3 show very high thermal stability in Ellingham's diagram, and the oxides of refractory metals such as W, Mo, Nb, and Ta (highlighted in yellow in Figure 9) typically have very negative reduction free energies (ΔG). They are low in position and the slope is small. This shows that these oxides have extremely high thermal stability. In Figure 9, Al_2O_3, Cr_2O_3, SiO_2, and TiO_2 are highlighted in orange. Among these oxides, the line of Al_2O_3 is at the lowest position, indicating that the oxide of aluminum is very stable. The Cr_2O_3 line is also low, but not as low as Al_2O_3, and it is higher than Nb_2O_5 and Ta_2O_5. The SiO_2 line is located between Cr_2O_3 and Al_2O_3, and the TiO_2 line is next to and below SiO_2. In general, the lines of refractory metal oxides are close to the lines of these metal oxides (Al_2O_3, Cr_2O_3, SiO_2, TiO_2), with only Al_2O_3 having the lowest position.

In Figure 9, oxides of transition metals Fe and Ni are highlighted in green. The Fe_2O_3 line position is relatively high, and the NiO line position is also high. Their oxides are not as stable as refractory metal oxides. This means that, compared to Fe_2O_3 and NiO, refractory metal oxides are more suitable for use in high-temperature environments.

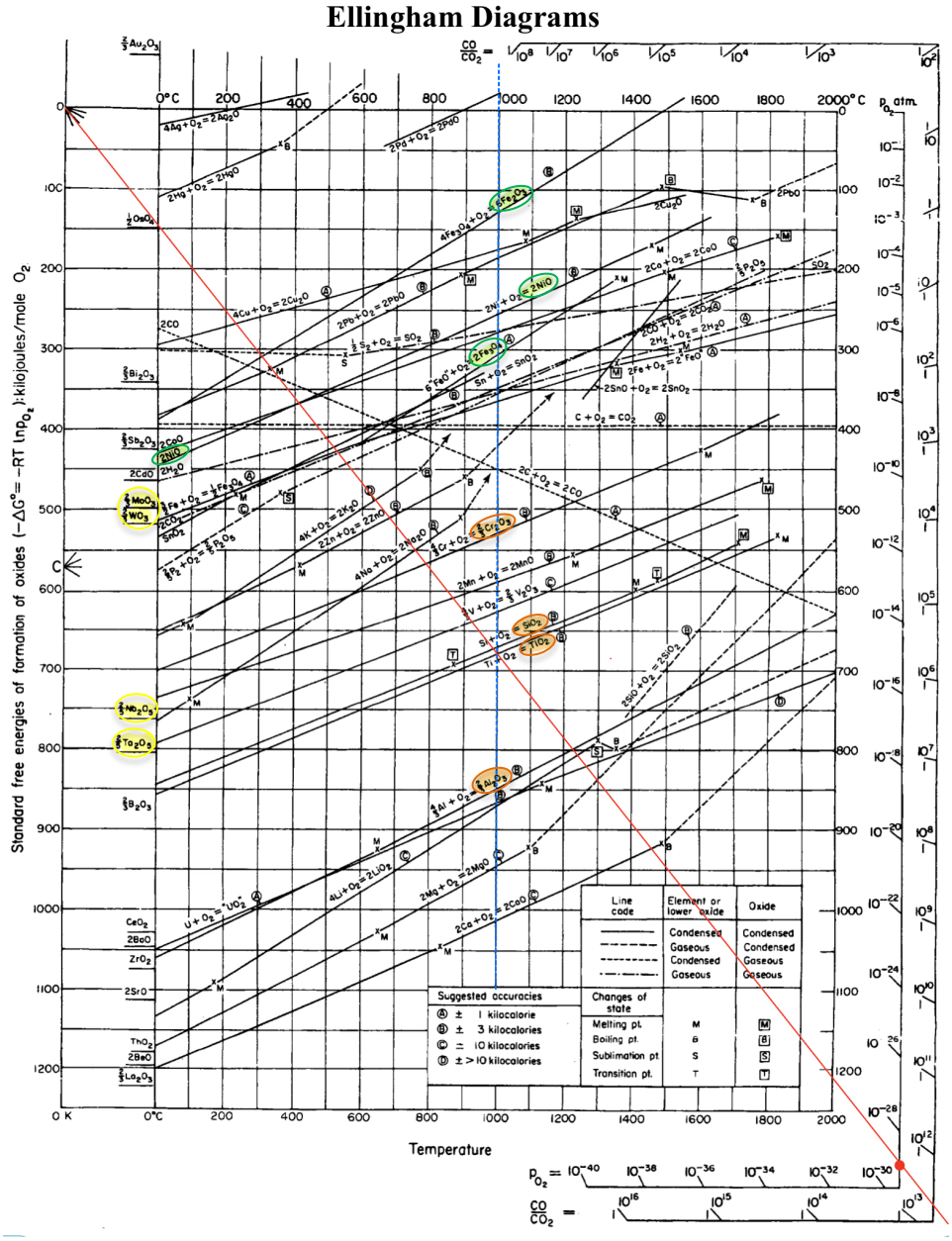

Figure 9. Ellingham diagram [37]

3.2 Kinetics of oxidation

Oxidation kinetics studies the rate at which oxidation reactions occur. It depends on factors such as the composition, temperature, pressure, and sometimes catalysts. This sub-chapter will introduce the Pilling-Bedworth ratio (PBR), transport mechanism, and linear, parabolic and logarithmic laws.

3.2.1 Pilling-Bedworth ratio and growth stress

A metal's ability to resist oxidation at high temperatures depends on the creation of a protective oxide layer, where the layer needs to be continuous to be able to resist further oxidation. Stresses within this oxide layer can lead to cracking and spalling, which directly impacts its integrity. Two main types of stresses that occur within the oxide layers are thermal stress and growth stress. The thermal expansion mismatch between the oxide layer and the metal substrate causes thermal stress. Growth stress arises during oxidation and is influenced by factors such as the volumes and crystal structures of the metal and oxide, and the oxide's growth mechanism [38]. The Pilling-Bedworth ratio (PBR) expresses the volume change resulting from the oxide formation at the metal/oxide interface:

$$PBR_{metal} = \frac{Volume\ of\ oxide}{Volume\ of\ metal}$$

When the Pilling-Bedworth ratio (PBR) is greater than 1, compressive stress will occur, and it usually means the formation of a flaking oxide on the surface. When the PBR is less than 1, tensile stress will occur, which usually means the formation of porous oxide. When the PBR is approximately 1, this usually means the formation of a dense and continued oxide, i.e., a protective oxide. PBR is often used to explain stress generation during oxidation and has served as the basis for some recent growth stress models. The PBR was originally used for metal oxidation, but it is an alloy that is widely used as a high-temperature material in practical applications. From Wagner's classification [39], alloys can be divided into two types: one with a base metal as the parent containing base alloying elements, and the other with a noble metal as the parent containing base alloying elements. For alloys containing two base metals, it is assumed that the oxide of one metal is more stable than the oxide of the other metal. This phenomenon occurs in many industrial alloy systems such as Fe-Cr, Ni-Al, and Fe-Al alloys. In a binary alloy where one metal is noble and the other is base, only the base metal oxidizes to form oxide during oxidation. Xu et al. have concluded a calculation method for PBR of the alloy oxidation [38]:

$$PBR_{alloy} = \frac{Volume\ of\ a\ mole\ of\ B_xO_y}{Volumeof\ x\ moles\ of\ B\ in\ alloy}$$

Table 1 shows the Goldschmidt ionic radius (A), which represents the ionic size of the element. The change in free energy of the oxidation reaction (ΔF), measured in kcal per gram of oxygen atoms at 1300K, is used to characterize the driving force of the oxidation reaction. The melting point and boiling point (℃) indicate the thermal stability of the oxide. Electrical conductivity (ohm^{-1} cm^{-1} at 20℃), indicating the electrical conductivity of the oxide. Oxide-metal volume ratio (PBR), which indicates the change in the volume of the metal after it is converted to an oxide. The PBR values of oxides of many common metals are listed in the table. Metals with a higher PBR, such as Nb and Mo, will form larger oxides during oxidation and may be more prone to cracking or peeling.

Table 1: PBR of different metals [40]

Element	Valence	Goldschmidt Ionic Radius, A	Oxide Properties: -ΔF at 1300 K, kcal per g atom of oxygen	Melting Point, C	Boiling Point, C	Conductivity at 20 C, $ohm^{-1}\,cm^{-1}$	Oxide-Metal Volume Ratio
Mn	2	0.80	69.3	1790	--	1×10^{-8}	1.79
Zr	4	0.79	101.4	2715	--	$<10^{-8}$	1.56
Co	2	0.72	33.3	1810	--	1×10^{-2}	1.86
Ni	2	0.69	28.6	1960	--	8×10^{-4}	1.65
Nb	5	0.69	63.9	1460	--	1.2×10^{1}	2.69
Ta	5	0.68	70.8	>1900	--	1×10^{-5}	2.54
Ti	4	0.68	84.8	1860	--	4×10^{0}	1.73
Fe	3	0.64	39.0	--	--	2.1×10^{1}	2.14
Cr	3	0.63	63.6	2440	--	1.2×10^{-4}	2.07
Mo	6	0.62	35.5	795	1460	1.3×10^{-7}	3.24
W	6	0.62	41.3	1470	1750	5×10^{-2}	3.35
V	5	0.59	49.6	660	--	3×10^{0}	3.19
Re	7	0.56	21.6	266	363	$<10^{-8}$	1.67
Al	3	0.50	100.3	2020	--	$<10^{-8}$	1.49
Si	4	0.41	77.2	1713	--	$<10^{-8}$	2.21
Be	2	0.35	112.8	1283	--	$<10^{-8}$	1.68
B	3	0.23	76.5	450	--	$<10^{-8}$	2.02

3.2.2 Coefficient of thermal expansion (CTE) and thermal stress

This sub-chapter will briefly introduce the coefficient of thermal expansion (CTE) and thermal stress, and their roles in high-temperature oxidation of alloys. Metals and alloys undergo dimensional changes as temperature changes, which has a significant impact on industrial processes such as casting, forging, and rolling. These dimensional changes may introduce residual stress, deformation, and even cracks that affect the product quality.

CTE describes the fraction of the change in length (or volume) caused by a change in temperature per unit. The coefficient of linear thermal expansion (α) can be calculated using [41]:

$$\alpha = \frac{1}{L}\frac{dL}{dT}$$

where L is the initial length and $\frac{dL}{dT}$ is the rate of change of length with temperature. The unit is K^{-1}. Metals and alloys generally have CTE values ranging from 10×10^{-6} to 30×10^{-6} K^{-1}, while ceramics exhibit lower values. Refractory metals in general have a low CTE. The CTE is temperature-dependent and usually increases continuously with temperature. However, phase transitions such as the ferrite-to-austenite transformation in iron-based materials can cause CTE discontinuities. Various numerical formulae exist for calculating CTE, either over a temperature range or at a specific temperature, leading to different definitions such as the mean coefficient of expansion α_m and instantaneous expansion coefficient α_I [41]. The coefficient of linear thermal expansion of some refractory metals as a function of testing temperature is shown in Figure 10 [42]. Nb shows the highest linear coefficient of thermal expansion and continues to rise with temperature, approaching 9×10^{-6} $m\cdot m^{-1}\cdot K^{-1}$ at 1400℃. The linear thermal expansion coefficient of Ta is slightly lower than that of Nb, and it remains relatively stable and increases slightly with the increase of temperature. The linear thermal expansion coefficients of Mo and W are low, where the value of W is the smallest, and there is almost no significant change over the entire temperature range. When working in high-temperature environments, selecting materials with low coefficient of thermal expansion can reduce the generation of thermal stress and prevent structural damage.

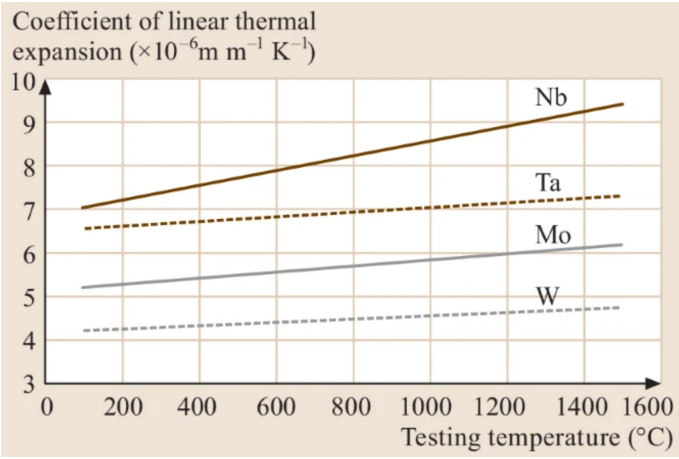

Figure 10: The coefficient of linear thermal expansion of some refractory metals as a function of temperature [42]

Thermal stress occurs when temperature changes cause differential expansion or contraction, and these deformations are restrained. Thermal stress (σ) can be calculated using:

$$\sigma = E \cdot \alpha \cdot \Delta T$$

where E is the elastic modulus, α is the CTE, and ΔT is the temperature change.

There are a variety of experimental techniques for measuring CTE at high temperatures. Common methods include mechanical dilatometry, which records dimensional changes as temperatures change; X-ray diffraction and optical imaging are also used. Each method has its limitations at extreme temperatures or in partially molten states. Models of casting and forging processes rely on precise CTE values to predict stresses and deformations during cooling. Using room-temperature CTE data in high-temperature applications can lead to errors. Therefore, high-temperature CTE data should be obtained from reliable references or through experimental measurements.

3.2.3 Linear, parabolic, and logarithmic laws

This sub-chapter will briefly introduce three principal laws: linear law, parabolic law, logarithmic law, and the corresponding mechanisms for these three laws during oxidation.

The mechanisms of oxidation are about the process of how ions and electrons move in the growing oxide layer, and possibly also in the defects inside. Regarding defects, usually it appears that Schottky defects and Frenkel defects are predominant. Schottky defects refer to the presence of equal amounts of cationic and anionic vacancies in the crystal structure, which is usually found in crystals such as alkali metal halides. In this case, to maintain electrical neutrality, it is necessary to assume that the same number or concentration of vacancies exist in both the cationic and anionic sublattices. Vacancies then exist in two sublattices so that both anions and cations will be mobile. Frenkel defect refers to the situation where only the cation is moving. Assuming that the anion lattice is perfect, the cation lattice contains an equal number of cation

vacancies and interstitials to maintain the electrical neutrality of the entire crystal [35]. This defect is found in crystals such as silver halides, where cations are free to migrate to vacancy and interstitial positions.

$$M(s) + \frac{1}{2}O_2(g) = MO(s)$$

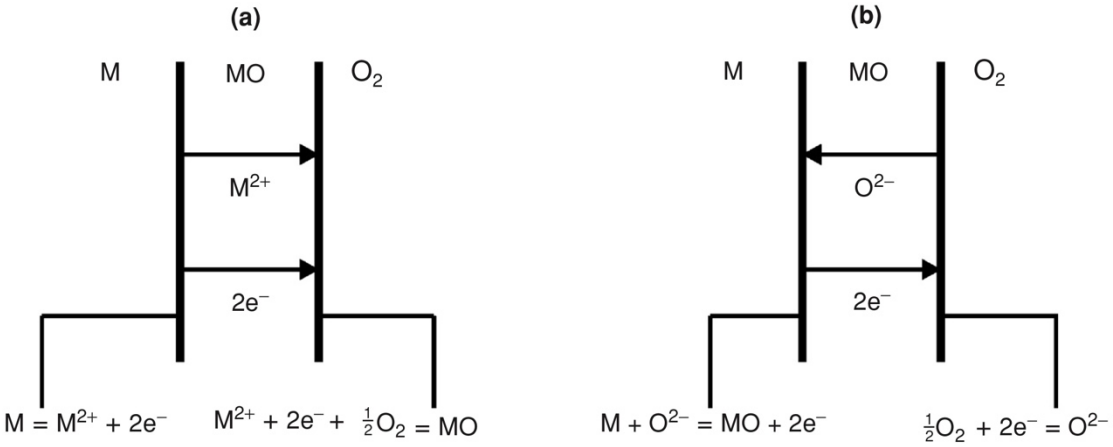

Figure 11: Interfacial reactions and transport processes for high-temperature oxidation mechanisms: (a) cation mobile and (b) anion mobile [35]

As shown in Figure 11 [35], the reaction must undergo the migration of neutral atoms, ions, and electrons. The transportation step relates to two interfacial reactions: the oxidized skin to the gas interface and the metal to the oxidized skin interface. An important difference exists between the two different scale growth cases: when the cation migrates, the oxidizing layer forms at the interface between the oxidizing layer and the gas, and when the anion migrates, the oxidizing layer forms at the interface between the metal and the oxidizing layer.

The *linear law* of oxidation describes the situation where the rate of oxidation remains constant over time. This means that the oxide layer grows at a uniform rate. It is expressed as $\Delta x = kt$, where Δx is the thickness of the oxide layer, k is a constant, and t is time. The linear law usually occurs when a surface reaction, such as a direct reaction of a material with oxygen controls the oxidation process. This often occurs in the initial stage of oxidation, when the oxide layer is thin and has no apparent resistance to the diffusion of the reactants.

The *parabolic law* of oxidation describes how the rate of oxidation decreases with time. This is because the growing oxide layer acts as a barrier to further oxidation, slowing down the oxidation process. It is expressed as $(\Delta x)^2 = kt$. It usually occurs when the diffusion of ions or atoms through the oxide layer is the rate-limiting factor, i.e., when diffusion through the oxide scale is the main factor controlling the rate. The thicker the oxide layer, the harder it is for the reactants to penetrate, slowing down the oxidation rate. This is a common condition for many metals and alloys at moderate temperatures.

The *logarithmic law* of oxidation describes a situation in which the rate of oxidation begins to decline rapidly and then gradually slows down over time, usually approaching a steady state. It is expressed as $\Delta x = k\ln(1+t)$. The logarithmic law is usually observed when very thin oxide films are formed at low temperatures. This suggests that the oxidation process is highly self-limiting, possibly due to the passivation of the surface by the initial oxide layer, which greatly inhibits further oxidation [43].

These three laws reflect the different mechanisms and stages of oxidation and provide insights into the protective properties of the oxide layer and the conditions under which it forms and grows. The schematic expression of the three laws is shown in Figure 12.

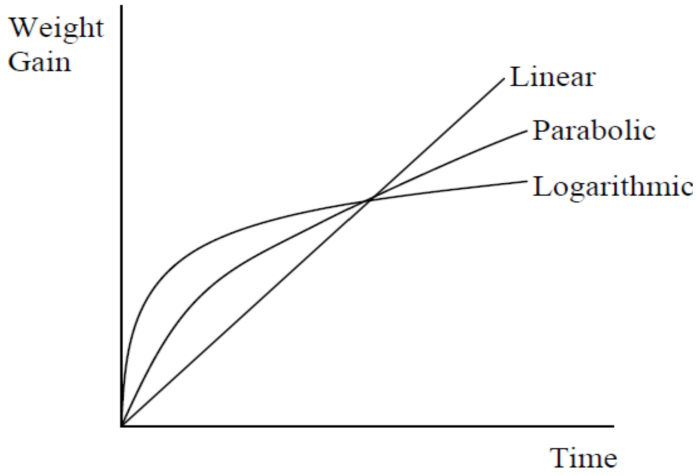

Figure 12: Common kinetics laws for the rate of growth of an oxide layer [44]

These three laws do not always occur exclusively. Sometimes different laws can occur in the same oxidation reaction. For example, some alloys upon oxidation at 1000℃ in air initially follows the parabolic law due to diffusion-controlled oxide layer growth. However, over time, it transits to a linear law, caused by the breakdown or spallation of the oxide layer, leading to a constant oxidation rate [26]. There are also transitions from linear to parabolic kinetics. Thin oxidizing layers with constant rate kinetics are often observed in oxidation reactions. When the formed oxidized layer is very thin, diffusion through the oxidized layer is rapid, and the metal activity at the oxidized scale-gas interface is initially maintained at a high level through rapid diffusion within the peroxide layer. As the reaction progresses, the oxidizing layer will gradually thicken. To maintain the constant ion flux through the oxidized layer, the activity of the metal at the interface between the oxide layer and the gas decreases with the thickening of the oxide layer, eventually approaching the equilibrium value with the atmosphere. The further thickening of the oxidized layer will decrease the metal activity gradient across the oxidized layer, reducing the ion flux and reaction rate. During the reaction process, as the oxidizing layer thickens, the main factor controlling the reaction rate changes from the initial surface reaction step or gas phase diffusion to ion transport within the oxidizing layer. The reaction rate will gradually decrease with time according to the parabolic law.

4 Oxidation of refractory alloys

Refractory alloys are alloys with main components based on refractory elements such as Mo, Ta, Nb, Ta, V, W, and Hf. As mentioned above, their poor oxidation resistance at HT has limited their applications. Researchers around the world are currently trying to address this issue. This chapter will showcase some interesting examples in this field.

4.1 Conventional protective scales

A conventional protective scale is a simple oxide formed on the surface of a metal or an alloy, composed of only one metal oxide, typically Al_2O_3, Cr_2O_3, or SiO_2. They have relatively low diffusion rates of metal and oxygen during oxidation, so their oxidation rates can be maintained at acceptably lower levels. Generally, under isothermal conditions, Cr_2O_3 oxide can provide maximum protection of about 1000-1100°C; Al_2O_3 up to about 1400°C; SiO_2 up to about 1700°C. However, a complicating factor for both Cr_2O_3 and SiO_2 scales is volatility, especially in environments with the presence of water vapor, which can significantly reduce the maximum-use temperature by several hundred degrees [7].

When an Al-containing alloy is exposed to a high-temperature oxidation environment, Al could selectively react with oxygen to form Al_2O_3. Al_2O_3 has thermodynamic stability at high temperatures and can resist oxidation. Its formation energy is lower than that of many other oxides, as introduced in the previous chapter about the Ellingham diagram, which helps to maintain the oxide layer integrity under extreme conditions. Al_2O_3 has relatively low rates of diffusion for both oxygen and metal ions. This characteristic slows down further oxidation by creating a barrier that significantly reduces the inward diffusion of oxygen and the outward diffusion of metal ions.

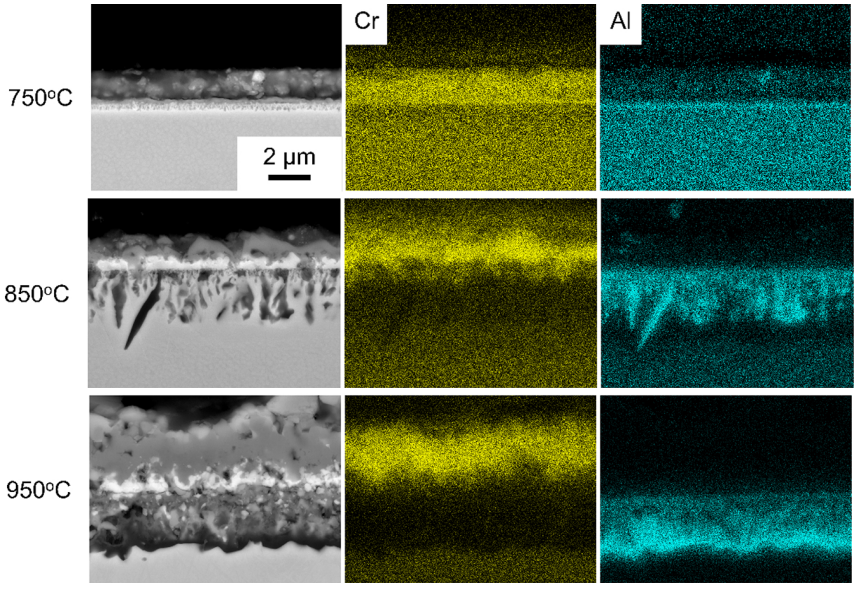

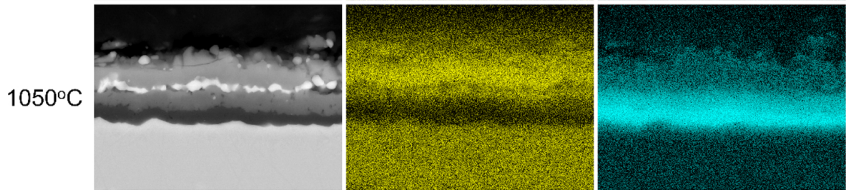

Figure 13. Representative BSE SEM images of the cross-sections from a Ni-based superalloy (Al (11.30 at%) and Cr (12.74 at%)) after exposure to air from 750 to 1050 ℃ (left). Corresponding EDX elemental concentration maps for Cr and Al are provided in addition to the BSE SEM images (right)[45] .

Therefore, the formation of a continuous, stable Al_2O_3 protective layer can achieve the effect of oxidation resistance at high temperatures, and sufficient Al concentration is required in the alloy. Ni-based superalloys, for example, have a continuous Al_2O_3 layer that acts as a barrier to prevent further oxygen penetration into the alloy. Figure 13 shows BSE and EDX images of cross-sections from a Ni-based superalloy under oxidation at different temperatures. With the increase of temperature, the oxide layer gradually thickens. At 750℃, the oxide layer is thin and uniform, and the distribution of Cr and Al are relatively concentrated, especially Al near the top of the oxide layer. At 850℃, the oxide layer begins to thicken and shows some irregular structure, but the whole layer remains intact. The further widening of Al distribution indicates that more Al_2O_3 is forming. At 950℃, the Al_2O_3 protective layer becomes thicker and effectively prevents further oxidation. At 1050℃, the oxide layer thickens significantly, but importantly, the Al oxide layer maintains its structural integrity at this temperature, with no significant cracks or pores. Figure 14 shows the 100-hour oxidation kinetics curve of the Ni-based superalloy (Al content 11.30 at%, Cr content 12.74 at%) obtained by thermogravimetric analysis (TGA). The green curve represents the experimental data (mass gain due to oxidation), and the dashed pink curve is the corresponding fitting model. The fitting results follow the parabolic law, so the oxidation process is controlled by diffusion. During the oxidation process, a protective oxide layer is formed on the surface of the alloy, and the oxidation rate slows down gradually with the thickening of the oxide layer. Unlike the Cr_2O_3 oxide layer, which may form volatile compounds like CrO_3 at high temperatures, the Al_2O_3 oxide layer remains solid and stable at high temperatures (above 1000℃), maintaining the integrity of the protective layer [45]. The stability and protection of the Al_2O_3 protective layer extend the service life of Ni-based superalloys in harsh high-temperature environments, such as turbine engines and aerospace applications.

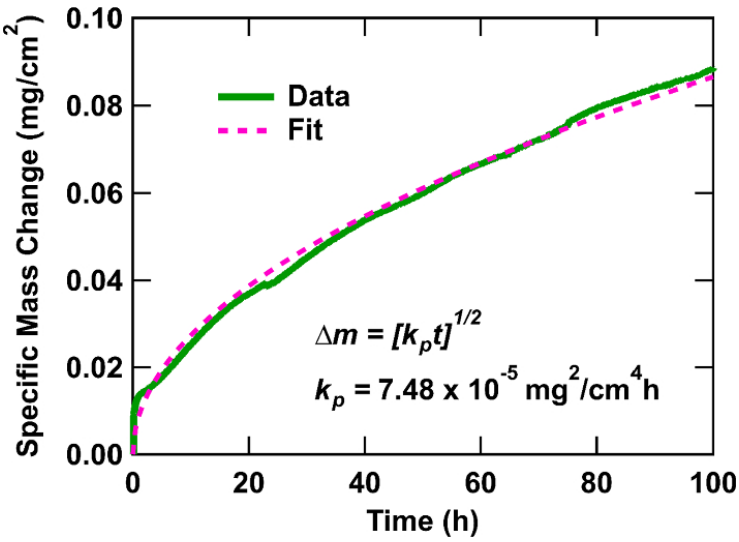

Figure 14. TGA-specific mass change results for a Ni-based superalloy (Al (11.30 at%) and Cr (12.74 at%)) during oxidation at 800℃ for 100 h in the air (green) and the corresponding fit (pink) [45]

For the Cr_2O_3 scale, a good example showcasing its role is with 316L stainless steels (mainly composed of Fe, Cr, and Ni). The main reason stainless steels have stainless properties is that they contain Cr [46]. Figure 15 shows the SEM image of the Cr_2O_3 scale formed on the top of a 316L stainless steel under elevated temperatures. When the stainless steel is exposed to oxidation, the Cr element reacts with oxygen to form a dense Cr_2O_3 protective film. It is very dense and can effectively prevent oxygen and other corrosive media from penetrating the interior of the stainless steel. Figure 16 describes the corrosion kinetics of a stainless steel 316L (left) and a P265GH steel (right) in contact with adipic acid at different temperatures (corrosion speed changes with time). The diagram on the left shows the corrosion behavior of the stainless steel 316L: at three different temperatures, the corrosion speed increases with the temperature. The corrosion speed of T3 was significantly higher than that of T1 and T2 and gradually stabilized after reaching a peak value at about 200 hours. The figure on the right shows the corrosion behavior of the P265GH steel: compared with 316L, the initial corrosion speed of P265GH is faster, but with the extension of time, the corrosion speed gradually decreases and tends to be stable. The corrosion speed of T3 was initially higher than that of T1 and T2, but eventually it reached a similar level after more than 400 hours.

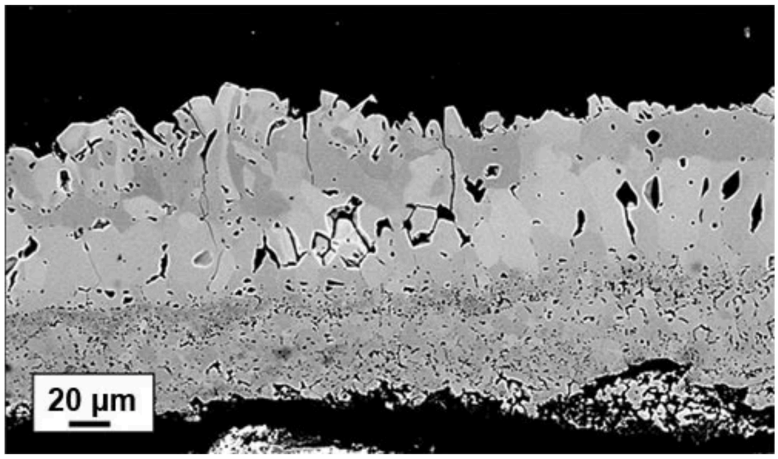

Figure 15. BSE micrograph of an oxide scale formed on a 316L stainless steel after four hours of exposure at 1200℃ [47]

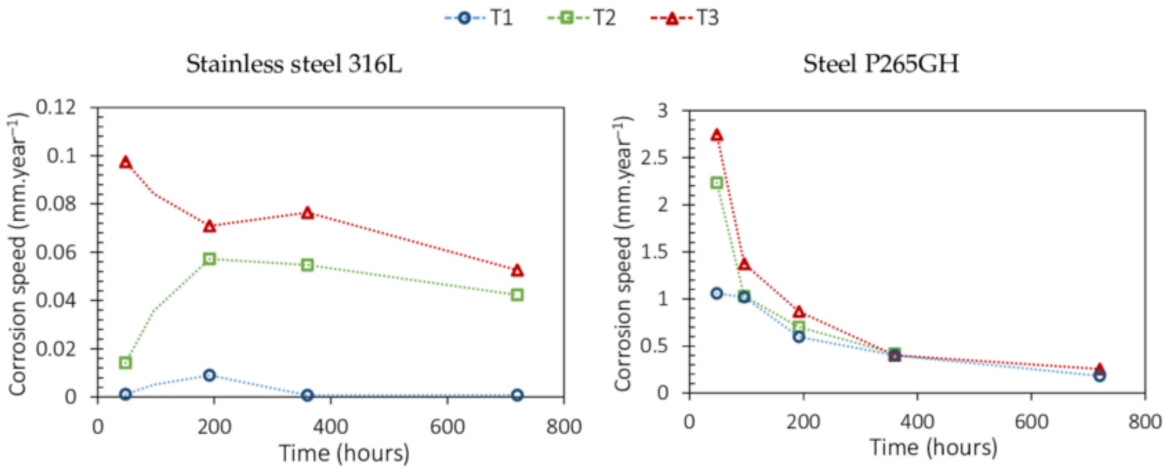

Figure 16: Corrosion kinetics of a stainless steel 316L (left) and a P265GH steel (right) in contact with adipic acid at 3 different temperatures (T1 = 166℃, T2 = 176℃, and T3 = 186℃) [48]

Under a high-temperature oxidation environment, Si in the MoSiB-based alloys combines with oxygen to form the SiO_2 scale. This process is thermodynamically favorable at temperatures around 1300℃ and SiO_2 scale forms more rapidly than other protective oxides such as Al_2O_3. SiO_2 has superior high-temperature thermodynamic stability, and a continuous dense layer of SiO_2 can effectively prevent oxygen diffusion, thus significantly reducing the rate of further oxidation, as shown in Figure 17. It is clear to see from the SEM images that there is a dense layer of SiO_2 having formed on the top of the alloy after certain hours under high temperatures. Unlike MoO_3, which is volatile at high temperatures, SiO_2 remains solid and stable, reducing mass loss and maintaining the integrity of the protective layer [49].

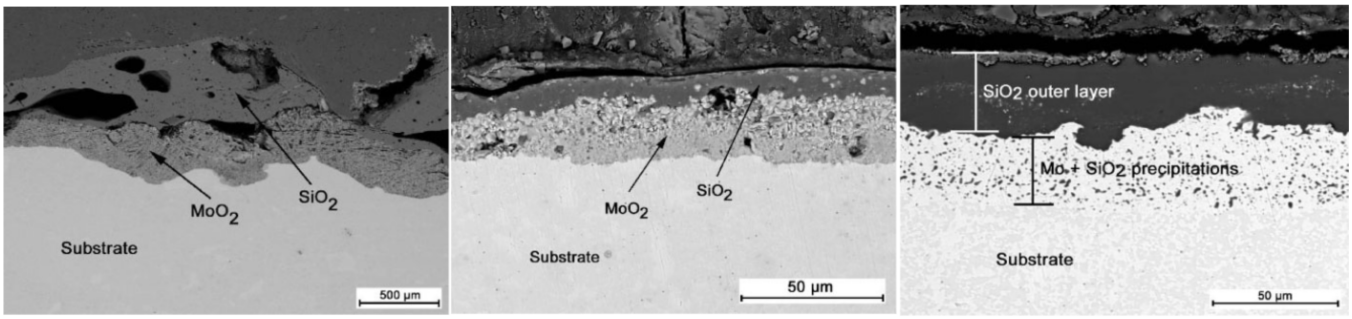

(1) (2) (3)

Figure 17. BSE image of Mo–9Si–8B cross-sections after (1) 7 h of oxidation at 820℃ and (2) 5 min of oxidation at 1100℃ and (3) 72 h of oxidation at 1300℃ [49]

MoSiB-based alloys containing intermetallic compounds such as Mo_3Si and Mo_5SiB_2 (T2 phase) exhibit complex oxidation behavior, mainly due to the interaction between different phases and the formation of complex oxides. During the initial oxidation stage, significant mass loss occurs due to the volatilization of MoO_3. This is critical as it can lead to rapid degradation of the alloy if a protective SiO_2 scale does not form quickly. At moderate temperatures (about 750℃), B_2O_3 can form a glassy phase with SiO_2, helping to reduce oxidation kinetics. At high temperatures around 1300°C, although B_2O_3 has a higher volatilization rate, it helps to form a continuous SiO_2 layer. The previous studies also pointed out that the oxidation resistance of MoSiB alloys can be further improved by adding La_2O_3 or Zr. La_2O_3 helps enhance the adhesion of the oxide scale and stabilizes the oxide film. This effect is significant in the temperature range between 800℃ and 900℃, helping to solve the oxidation problem of conventional MoSiB alloys in this temperature range. The addition of Zr forms a finer microstructure which can help to reduce initial mass loss at temperatures around 1100℃ [49]. The oxidation behavior of Mo-Si-B alloy at high temperatures is shown in Figures 18 (a) and (b), showing the formation of different oxides at different temperatures and the change of mass/ thickness with time. Figure 18 (a) shows the weight change of Mo-9Si-8B alloy at different temperatures and times. As the temperature increases, the weight loss of the alloy increases significantly, especially at higher temperatures (1100℃ and 1300℃), where the oxidation rate is much higher. Figure 18 (b) is the oxide thickness change of SiO_2 and MoO_2 oxides with time at 1100℃ and 1300℃. With the increase in temperature, the oxide layer thickness increases significantly, especially at 1300℃, where the thickness of SiO_2 increases rapidly, and the final thickness is much higher than the oxide layer formed at 1100℃.

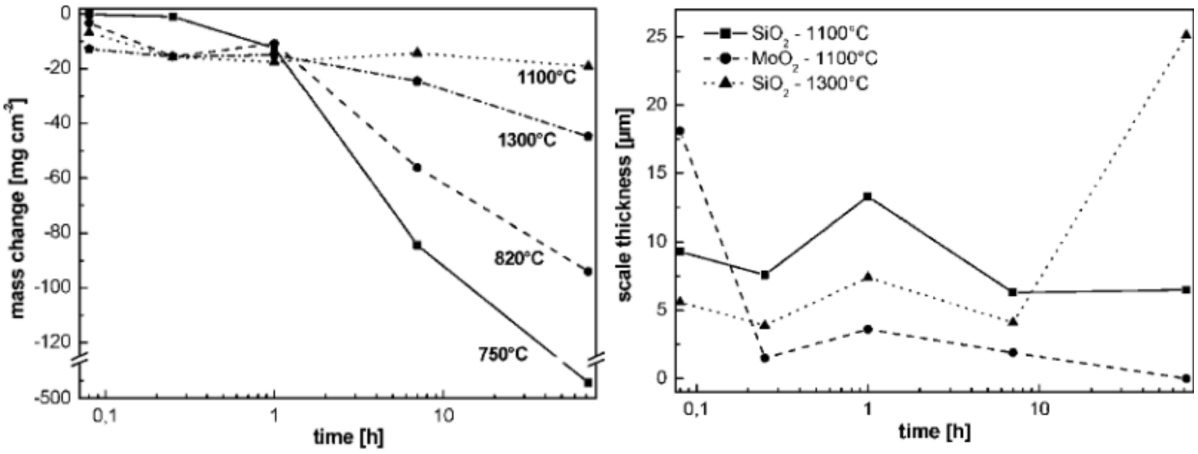

(1) (2)

Figure 18. (1) Weight change versus time plot for a conventional Mo–9Si–8B alloy (2) Oxide scale thickness of SiO_2 and MoO_2 at 1100 and 1300℃ [49]

Sheikh et al [50]. used a two-step pack aluminizing strategy to form a protective Al_2O_3 scale on the surface of a ductile RHEA ($Al_{0.5}Cr_{0.25}Nb_{0.5}Ta_{0.5}Ti_{1.5}$) under HT. Two-step aluminizing is a coating process designed for Ti-rich alloys that consists of two stages: high temperature, low activity aluminizing to form a TiAl layer, and then low temperature, high activity aluminizing to form a top $TiAl_3$ layer. This method created a layered structure with $TiAl_3$ on the surface and TiAl underneath, with a diffusion zone between TiAl and the substrate. The results showed that it successfully formed a protective Al_2O_3 layer upon oxidation, as shown in Figure 19.

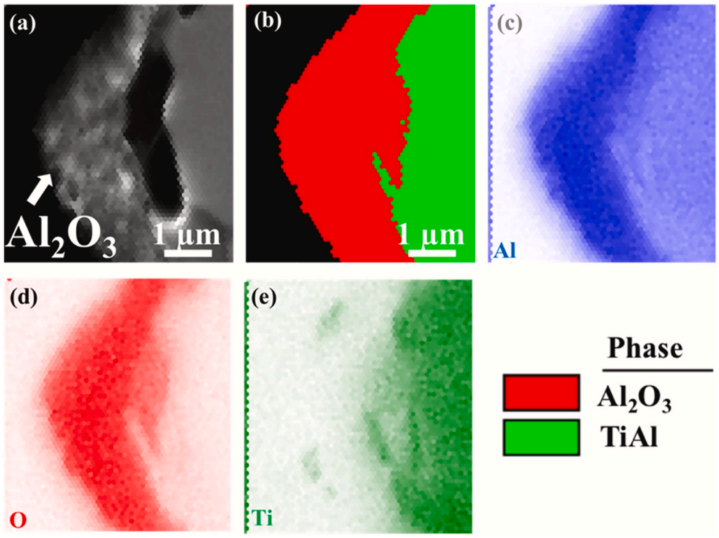

Figure 19. Formation of Al_2O_3 scale on the surface of an aluminized $Al_{0.5}Cr_{0.25}Nb_{0.5}Ta_{0.5}Ti_{1.5}$ RHEA, after 20 cycles of oxidation tests: (a) SEM backscattering electron image; (b) EBSD phase map; (c)–(e) EDS elemental maps for the area in (a) revealing the distribution of Al, O and Ti, respectively, at the cross-section

The formation of conventional protective oxide layers such as Al_2O_3 could be an effective way to improve the oxidation resistance of RHEAs. However, over the past years, it has become clear that it is rather difficult to form a pure Al_2O_3 scale that is dense and continuously protective on the surface of RHEAs. Usually, complex protective scales without sufficient oxidation protection are formed. Research work on

the protective oxide formation in RHEAs is still ongoing, aiming to improve the oxidation resistance of RHEAs.

4.2 Pesting

Pesting, or pest disintegration, is a catastrophic phenomenon in certain high-temperature materials such as $MoSi_2$, berylliums, and aluminides. Although these materials have excellent oxidation resistance at high temperatures, decomposition occurs in certain temperature ranges. The phenomenon was first observed in 1955 [51]. The exact mechanism of pesting is not fully understood and varies in different alloy systems. As an example, the pesting mechanism of $MoSi_2$ will be explained in this sub-chapter.

$MoSi_2$ is considered suitable for structural applications above 1200°C due to its high melting point (2020°C), excellent oxidation and corrosion resistance, good thermal conductivity, and high strength. It exhibits brittleness at low temperatures and decreases in strength at high temperatures. Pesting in $MoSi_2$ occurs when the material is exposed to a temperature range of 300-500°C, leading to its disintegration into powder, which can be observed in Figure 20. This phenomenon is likely due to grain-boundary embrittlement caused by oxygen diffusion. At these temperatures, $MoSi_2$ reacts with oxygen to form MoO_3 and SiO_2. MoO_3 grows rapidly inward, continuously removing SiO_2 nuclei. Mixtures of MoO_3 and SiO_2 have low adhesion and compatibility, causing the poorly attached oxides to fall off as fine particles, exposing the material to oxygen and repeating the process [52]. At higher temperatures, transient MoO_3 evaporates, allowing a continuous protective SiO_2 layer to form and prevent pesting. In Figure 20, experimental findings reveal that $MoSi_2$ samples oxidized between 375°C and 500°C disintegrate, while those oxidized at 350°C or above 600°C remain intact. At 500°C, the samples' color changed from metallic to greenish-gray and eventually yellow after a long time of oxidation. The resulting powder mainly consists of MoO_3, SiO_2, and residual $MoSi_2$ [53], following the reaction:

$$2MoSi_2(s)+7O_2(g)\rightarrow 2MoO_3(s)+4SiO_2(s)$$

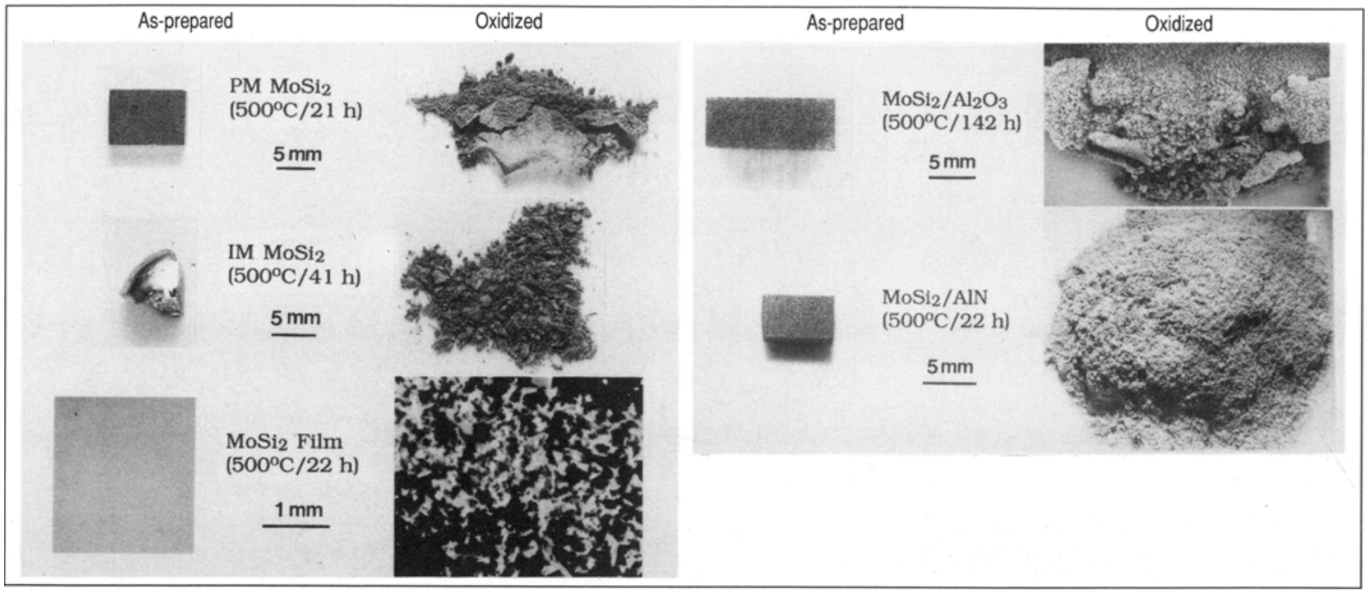

Figure 20. SEM micrographs showing the morphological characteristics of various $MoSi_2$ samples after oxidation at 500℃ for different periods. PM-powder metallurgy; IM-ingot metallurgy [53]

Pesting is characterized by an initial slow oxidation phase, followed by a rapid disintegration phase, finally leading to complete material disintegration. Pesting also occurs in various refractory silicides, where the rapid formation of refractory oxides prevents the formation of a continuously protective SiO_2 layer.

4.3 Complex protective scales

Compared with the conventional protective scale, the complex protective scale has a more complicated structure and chemical composition. They typically comprise more than one metal oxide. This kind of protective scale is usually easy to obtain and sometimes undesirable because of the defects and spallation.

Gorr et al. [54] studied a RHEA system Mo–W–Al–Cr–Ti where the oxidation test was performed at 1000℃ for 40 hours in the air. They tried to form the Al_2O_3 protective scale, however, the result showed that the growth of the oxide scale was carried out by solid diffusion and the oxidation rate was high. Earlier, Becker et al. [55] found out that alloys containing Nb can form the protective Al_2O_3 layer, so in this case they hypothesized that replacing Ti with Nb in the alloy Mo-W-Al-Cr-Ti might help form a protective layer of Al_2O_3 on the metallic surface to enhance its oxidation resistance.

Anber et al. [56] studied the oxidation behavior of a HfNbTaTiZr RHEA with 4.8 and 13 at% of Al addition. They were trying to improve the oxidation resistance of these RHEAs by obtaining the Al_2O_3 scale on the surface. The samples undergo oxidization at 900℃ for 10h and 1100℃ for 20 hours in the air. However, the result showed that the oxide layer was not purely Al_2O_3. They concluded that Al addition caused the formation of complex oxides, i.e., Nb_2O_5, $Nb_2Zr_6O_{17}$, and Al_2O_3. They used the OQMD database to identify the oxides with large negative formation energy, i.e., HfO_2/ZrO_2, and oxides like these always formed near the metal/oxide interface. They proposed that when designing RHEAs, the contents of Zr and Hf shall be lowered to minimize their undesirable impact on alloy passivation and intermetallics formation.

Lu et al. [57] investigated the effects of Al content on the oxidation resistance of a RHEA system $Al_xMo_{0.5}NbTa_{0.5}TiZrl$, where x= 1, 1.25, 1.5. The oxidation test was carried out at 900 and 1000°C both for 0.5h and 10h in air. The result showed that oxidation resistance increased with the increasing Al content. However, there was still no pure Al_2O_3 scale formed, and instead the formation of $AlNbO_4$ and $AlTaO_4$ were thought to be beneficial to the alloys' oxidation resistance.

Zhang et al. [58] studied $Al_xCrTiMo$ (x=0.25, 0.5, 0.75, 1) RHEAs prepared by the spark plasma sintering method. They investigated the oxidation behavior of these alloys in air at 1000°C for 1h and 7h. The RHEAs with x = 0.5, 0.75, and 1 showed a medium oxidation rate, which was twice as slow compared to the RHEA with x = 0.25. The oxide layer consisted of TiO_2, Al_2O_3, and Cr_2O_3, from the exterior to the interior of the alloy, which rendered excellent protective properties. They believed that Al content plays a crucial role in the anti-oxidation properties of RHEAs. Alloys with high Al content are easy to form protective layers in a short time, so they have good oxidation resistance at high temperatures.

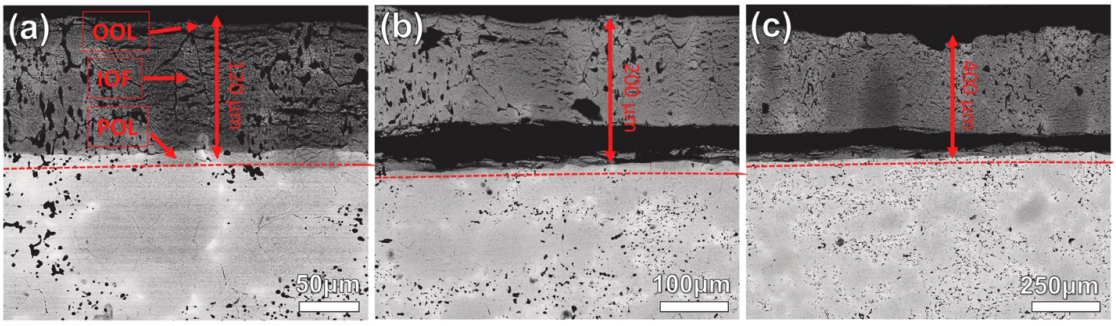

Figure 21. Cross-sectional BSE images of the WTaNbTiAl RHEA after oxidation at 1000℃ for 12 h (a), 24 h (b), and 48 h (c), respectively [59]

Yan et al. [59] developed a WTaNbTiAl RHEA and demonstrated its high-temperature oxidation behavior which was carried out at 1000 ℃ in air for 12h, 24h, and 48h. After 48 h of oxidation, a complex protective scale formed. They concluded that the WTaNbTiAl alloy showed excellent oxidation resistance by analyzing the oxidation products. The complex oxide layer as shown in Figure 21 contained an outer oxide layer (OOL) that mainly consisted of $AlNbO_4$, Ti-rich oxides, $Ta_{1.5}Nb_{1.5}O_3$, an internal oxidation front (IOF), which mainly consisted of $Ta_8W_9O_{47}$ and other Ti-rich and Ta-rich composite oxides, and an internal "partially oxidized" layer (POL).

The oxidation behaviors of equiatomic NbTiZrV and NbTiZrCr alloys at 1000 ℃ in air were studied by Butler et al. [60] in 2017. The V-containing alloy completely oxidized after 8h and formed complex oxides including $TiNb_2O_7$, TiO_2, $Nb_2Zr_6O_{17}$, and V_2O_5. The Cr-containing alloy formed the oxides of $NbCrO_4$ and ZrO_2, which also did not exhibit sufficient protective properties. In 2022, the same authors studied the oxidation behaviors of CrNb, CrNbTi, and CrNbTaTi alloys at 1200 ℃ in air. The oxide layer of CrNb contained an outer layer of Cr_2O_3 and an underlying layer of $CrNbO_4$. The CrNbTi alloy formed an outer layer of Cr_2O_3 and an underlying layer of $NbTiO_4$. The CrNbTaTi alloy, however, did not form a sufficiently protective scale. The oxidized layer had a complex composition and had a high density of cracks and voids which experienced extensive spallation after a longer oxidation time.

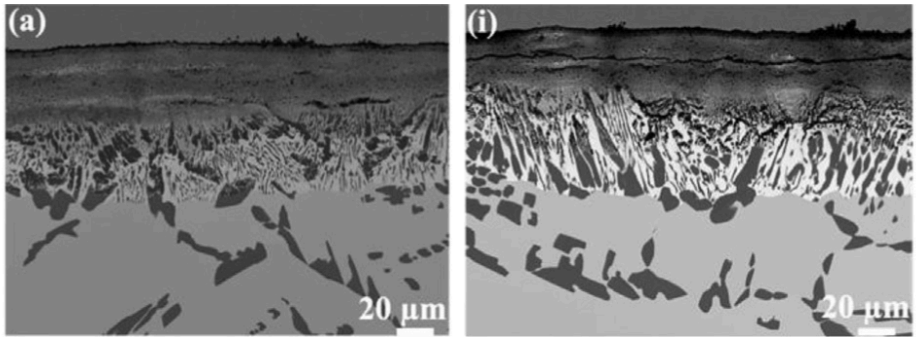

Figure 22. Cross-sectional microstructures of (a) $Al_{0.5}Cr_{0.25}Nb_{0.5}Ta_{0.5}Ti_{1.5}$, (i) $Al_{0.75}Cr_{0.25}Nb_{0.5}Ta_{0.5}Ti_{1.5}$ specimens after 100 h of exposure at 1100℃ [61]

Sheikh et al. [61] investigated the alloying effect on the oxidation behavior of a ductile RHEA $Al_{0.5}Cr_{0.25}Nb_{0.5}Ta_{0.5}Ti_{1.5}$ with two modified compositions. The two modified RHEAs, $Al_{0.75}Cr_{0.25}Nb_{0.5}Ta_{0.5}Ti_{1.5}$ and $Al_{0.5}Cr_{0.25}Nb_{0.5}Ta_{0.5}Ti_{1.5}Zr_{0.01}$, showed better oxidation resistance at 800℃ and 1100℃. Although none of them successfully formed a dense Al_2O_3 layer, a complex protective scale

was formed, and oxides like TiO_2, Ta_2O_5, and Nb_2O_5 appeared. Comparing the results of $Al_{0.5}Cr_{0.25}Nb_{0.5}Ta_{0.5}Ti_{1.5}$ and $Al_{0.75}Cr_{0.25}Nb_{0.5}Ta_{0.5}Ti_{1.5}$, as shown in Figure 22, the $Al_{0.5}Cr_{0.25}Nb_{0.5}Ta_{0.5}Ti_{1.5}$ RHEA formed the complex oxides containing a large amount of Nb_2O_5, which can cause the cracking and reduce the oxidation resistance, while the $Al_{0.75}Cr_{0.25}Nb_{0.5}Ta_{0.5}Ti_{1.5}$ RHEA had more Al_2O_3 forming on the surface, which suppressed the formation of Nb_2O_5. The results showed that Al alloying can have a remarkable effect in inhibiting oxygen ingress.

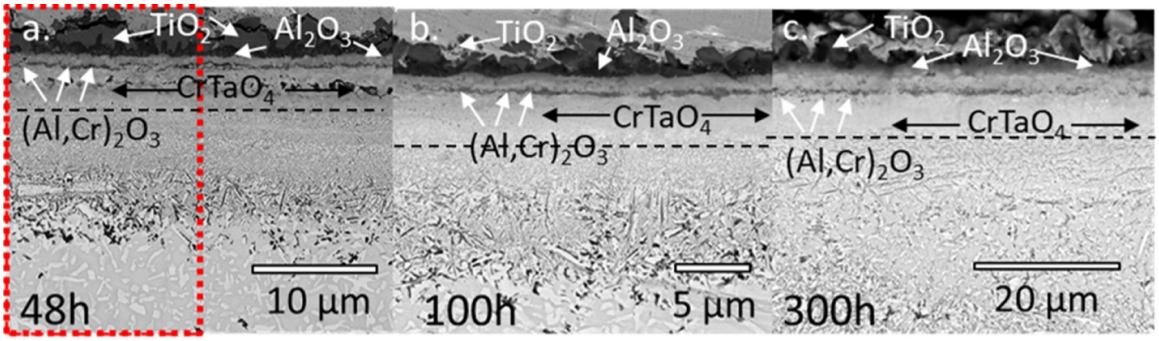

Figure 23. BSE images of TaMoCrTiAl after 48 h (a.), 100 h (b.) and 300 h (c.) of exposure to air at 1000℃ [62]

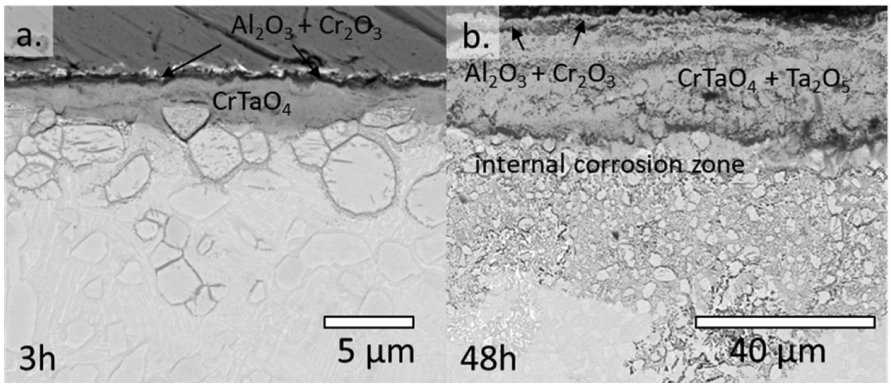

Figure 24. BSE images of TaMoCrAl after 3 h (a.) and 48 h (b.) of exposure to air at 1000℃ in air [62]

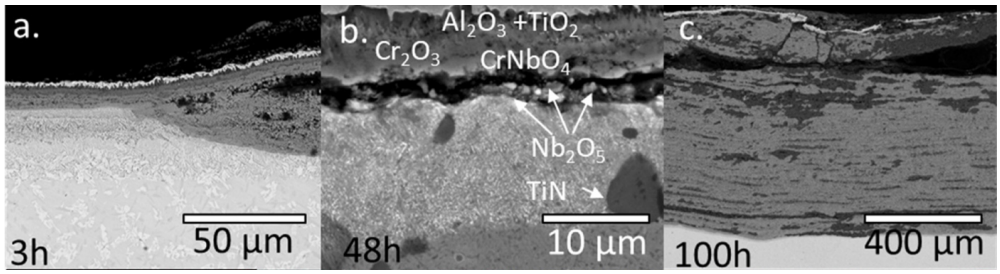

Figure 25. BSE images of NbMoCrTiAl after 3 h (a.), 48 h (b.) and 100 h (c.) of exposure to air at 1000℃ [62]

Müller et al. [62] investigated the mechanism of high-temperature oxidation in several RHEAs, TaMoCrTiAl, NbMoCrTiAl, NbMoCrAl, and TaMoCrAl at 1000℃ in air and the influence of elements such as Ti, Nb, and Ta on oxidation resistance. The results showed that the TaMoCrTiAl alloy had excellent oxidation resistance in air. They attributed this to the formation of protective layers of composite oxides, i.e., Al_2O_3, Cr_2O_3, and $CrTaO_4$, and the slow diffusion of oxygen by the $CrTaO_4$ layer, as shown in Figure 23. Figure 24 shows the outer layer of oxidized TaMoCrAl. It did not keep the protective $CrTaO_4$ layer when the oxidation time got longer; instead, it formed a porous complex oxide layer containing Al_2O_3, Cr_2O_3, $CrTaO_4$, and Ta_2O_5. Although a complex protective oxide layer composed of Al_2O_3, Cr_2O_3, and

$CrTaO_4$ was also formed in the Nb-containing systems, which were NbMoCrTiAl and NbMoCrAl, the strong anisotropic thermal expansion of the Nb_2O_5 polymorphs led to the formation of pores and spallation (Figure 25). The Nb-free and Ti-containing TaMoCrTiAl alloy formed a protective layer of rutile type oxides, e.g., CrTaO4, and the amount of undesired oxides, e.g., Nb_2O_5, Ta_2O_5 was reduced.

According to the available literature reports, although the formed oxide layer has different complex compositions, adding moderate Al in general improves the oxidation resistance by forming a protective scale mixed with Al_2O_3. Mo addition is not recommended due to the evaporation of oxidation products. As a more complex oxide form, the complex protective scale has a multifaceted impact on oxidation and corrosion protection. More effective methods are expected to be developed to enhance the oxidation resistance of RHEAs and promote their wide applications in high-temperature environments.

5 Experimental methods

Three carefully designed alloys Nb-15Hf-5.5W-4Al, Nb-15Hf-5.5W-8Al, and Nb-15Hf-5.5W-12Al were prepared by arc melting, followed by drop casting. This chapter describes the procedures of sample preparations, and microstructure and hardness investigations. The scope of the experiment may be limited by the number of alloys and the chosen oxidation conditions. In addition, achieving precise alloy compositions in the melting process of RHEAs is also challenging, especially due to the volatility of low-melting elements such as aluminum, which increases the difficulty of the sample preparation.

5.1 Sample preparation

The specimens were in the form of ingots with cross-section dimensions of about 10mm × 10mm. They were cut into cuboids with approximate dimensions of 4 mm × 4 mm × 4 mm by a precision saw with a diamond blade. The surfaces of each specimen were ground to a 1200-grit finish, ultrasonically cleaned in ethanol, and finally dried using a pressurized air stream. Before oxidation, the exact dimensions of each specimen were meticulously measured with a caliper, with a precision of 10^{-3} mm, and the surface areas of each cuboid were accurately calculated. Both pre- and post-oxidation samples were heat-mounted and prepared using standard metallographic methods for microstructural analysis. Figure 26 shows the sample preparation working area where all the relevant experiments were done.

Figure 26. Sample preparation area

5.2 Oxidation studies

In laboratory studies, the experimental technique of measuring oxidation kinetics for high-temperature oxidation is usually straightforward. The crucible with the sample inside was weighed before oxidation, using a highly sensitive balance (10^{-6} g). The crucible was then loaded into a ceramic tube furnace at desired temperatures, allowing it to oxidize for a certain amount of time. When the time was due, the crucible with the sample inside was removed from the furnace, cooled in the air, and then weighed again. A lid was in

place for the crucible to prevent any loss of oxides during the whole process and was weighed as a part of the crucible. The whole process is schematically shown in Figure 27. An oxidation kinetics curve will be obtained after a series of repetitions of this procedure under the same temperature, for different times. In this study, discontinuous oxidation tests of alloys were conducted in a ceramic tube furnace, being exposed to static laboratory air, at 800℃, 1000℃, and 1200℃ for 1h, 8h, and 24h. Assuming that the mass of the crucible remains constant, the mass gain of the sample can be calculated by comparing the mass before and after oxidation. To calculate the specific mass change, the mass gain by the initial specimen was normalized by the total specimen surface area. With the measured results of specific mass change, the oxidation kinetics curves were plotted, characterizing the specific mass gain (mg/cm^2) as a function of time (h).

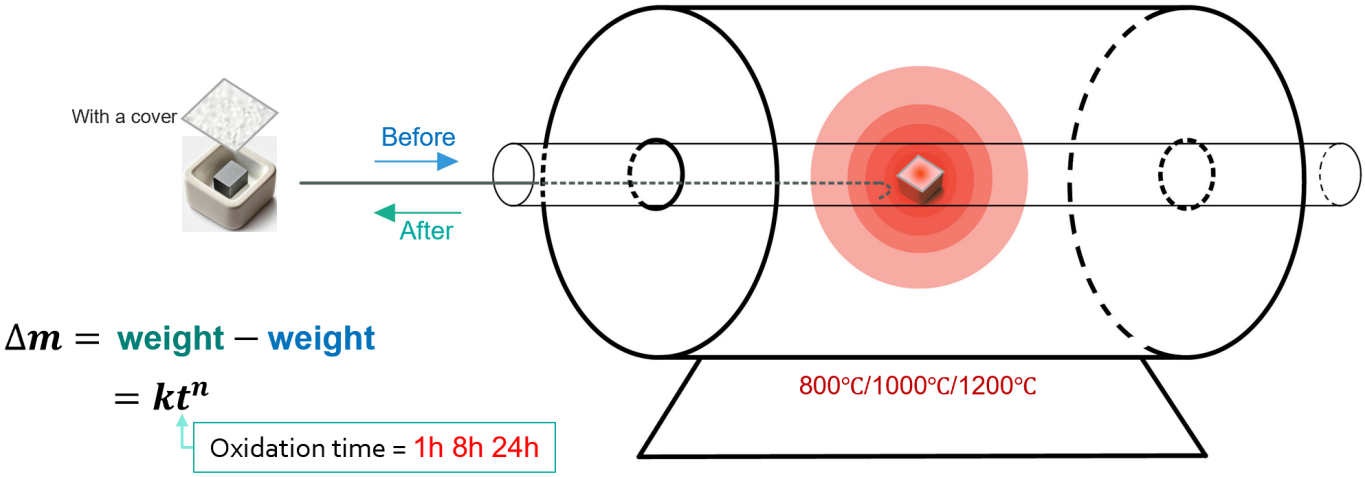

Figure 27. Illustration of the oxidation experiment process

5.3 Scanning electron microscopy

Scanning electron microscopy (SEM) is a microscope that uses electrons to form an image, to examine the surface morphology and composition of materials at high magnification. Figure 28 shows the SEM and EDS equipment used in this thesis. The electrons emitted from the gun are directed by a magnetic lens, whose current can be adjusted to alter the trajectory, intensity, and size of the beam. The scanning coils then precisely determine the position of the beam. Resolution is determined by the objective lens, regardless of its shape, and is positioned on a holder capable of movement in x, y, and z directions, as well as rotation and tilt. Finally, the detector collects the signal and translates it for analysis. In our case, the backscattered electrons (BSE) mode is used to observe the microstructure of polished alloy samples and the cross-sections of oxidized samples, and the secondary electrons (SE) mode is used to observe the sample surface defects and the oxidized sample surface [63]. SE are produced through inelastic interactions of high-energy electrons with valence or conduction electrons within the specimen, causing them to be ejected from the atoms, with energies below 50eV. Each incident electron can generate multiple SE. SE production is highly topography-related, only those within <10nm of the surface can exit the sample due to their low energy. Topographic contrast arises from the angle of incidence between the electron beam and the sample surface, with local variations in surface angle affecting emitted electron numbers, creating "topographic contrast." This contrast occurs because electrons emitted from surfaces not directly facing the detector encounter difficulty reaching it, resulting in darker appearances [63].

BSE is produced by elastic interactions between beam electrons and nuclei within the specimen, possessing high energy and large escape depth. BSE images provide atomic number contrast, as primary electrons create cascades deep within the sample, allowing BSE signals to convey information beyond the surface. BSE images contain both compositional and topographical information, identified by a paired semiconductor detector symmetrically placed relative to the optical axis. Addition of them shows a composition image, and subtraction shows a topography image. BSE yield varies with atomic number (Z), enabling clear distinction between different phases, with heavier elements appearing brighter. BSE yield (η) is a function of the atomic number, Z, resulting in atomic number contrast in BSE images, where higher average Z regions appear brighter, with η increasing with tilt [63].

SE typically offers a resolution equivalent to the size of the electron beam and is predominantly utilized in SEM applications. Conversely, BSE has a larger generation region than SE, resulting in BSEs providing lower spatial resolution than SE. In this study, SE is used to observe the topography of the oxidation and cutting surfaces of the post-oxidation samples, while BSE is employed to analyze the polished surfaces of both pre- and post-oxidation samples. SEM imaging was conducted with an applied voltage of 15kV and magnifications ranging from 200X to 1000X.

Energy dispersive X-ray spectroscopy (EDS/EDX) is used to show the elemental distribution from the SEM image. EDS/EDX detectors are attached to electron column instruments to analyze the elemental composition of a sample. It is capable of imaging and mapping in SEM, EPMA, or STEM, and it works by detecting the characteristic X-rays emitted by the specimen when bombarded by a focused electron beam. When the incident electrons interact with the atom's inner electrons, such as the K electrons, they may knock out them, leaving a hole. Later, higher energy L electrons will jump into this hole, resulting in the emission of X-rays. The energy levels of these X-rays are characteristic of the elements present in the specimen. A spectrum will be formed to determine the elemental composition and concentration within the specimen. EDS operates in various modes: point analysis provides signals from a single point (0D), line analysis scans along a line (1D) to show elemental distribution along it, area analysis provides an average chemical concentration in a defined area, and elemental map displays the distribution of each element in a given area (2D). EDS is often used in conjunction with SEM. In our case, it was used for the BSE image of the sample; point analysis was used for compositional analysis of different microstructures, and line and area analysis were used to detect composition variation in different regions [64].

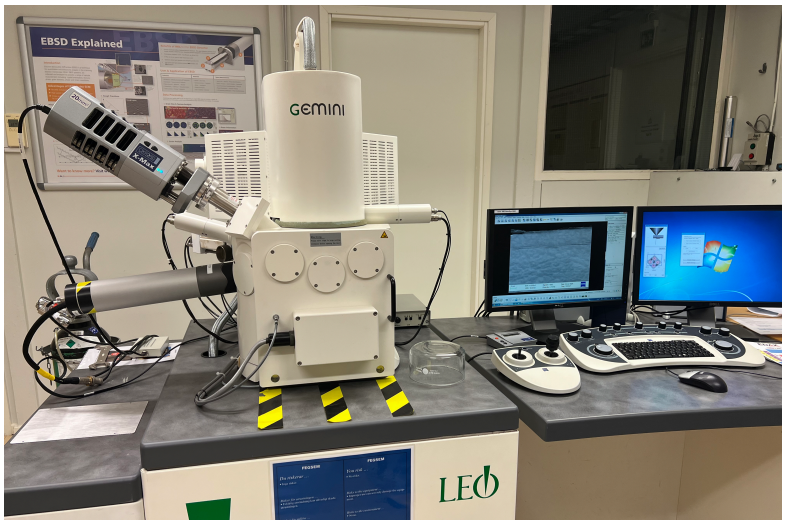

Figure 28. FEGSEM LEO-1550

5.4 X-ray diffraction

X-ray diffraction (XRD) is an analytical technique used to determine materials' crystallographic structure and phase identification. Figure 29 shows the XRD equipment used in this thesis. The crystal structures of the materials are analyzed using XRD with Cu-$K_{\alpha 1}$ radiation. In an XRD setup, X-rays caused by an external source are directed onto the crystal, where they are diffracted by the lattice planes into specific directions, and the resulting diffracted X-rays are collected by a detector. The angle and intensity of the scattered X-rays provide insight into the crystal structure of the sample, described by Bragg's law:

$$n\lambda = 2dsin\theta$$

where n is the diffraction order, λ is the wavelength of the X-ray source, d is the interplanar distance and θ is the diffraction angle. Each peak in the XRD pattern corresponds to a specific set of crystallographic planes within the material [65]. The crystal structure, phase composition, and crystalline size of the material can be determined by analyzing the positions and intensities of these peaks. In our case, the crystal structures of the oxides formed were analyzed using XRD with Cu-$K_{\alpha 1}$ radiation with $2theta(\theta)$ range from 20° to 80°. For the 1h oxidized samples, the bulk surface was used for XRD analysis since the oxides were still intact and attached to the surface. For the 8h and 24h oxidized samples, pesting was significant and off-spalled powders were used for XRD analysis.

Figure 29. XRD - Bruker D8 Discover

5.5 Hardness test

In this study, the Vickers hardness measurement was used. Figure 30 shows the Vickers hardness test equipment used in this thesis. It uses the diamond indenter with a pyramid geometry forced onto the surface of the polished sample, which can be used for macro and micro-hardness testing, with the load ranging from 10gf to 100kgf [66].

The hardness can be calculated as:

$$HV = 0.1891 \frac{F}{d^2}$$

where HV is Vickers hardness, F[N] is load, and d[mm] is the mean length of the diagonals of the indentation print.

In our case, all samples were tested with a load of 5kg, applied for 15s for each indent. Each mounted sample was polished to a flat surface during hardness testing, and 22 hardness measurements were taken randomly across the surface. The highest and lowest values were discarded, and the mean and standard deviation were calculated from the remaining data.

Figure 30. Vickers hardness test equipment

6 Results and discussion

6.1 Pre-oxidation: microstructure, hardness, and phase

Table 2. Chemical compositions of alloys, all in at%

Alloys	Nb	Hf	W	Al
Nb-15Hf-5.5W-4Al	75.6	15.1	5.8	3.5
Nb-15Hf-5.5W-8Al	70.3	17.5	4.5	7.6
Nb-15Hf-5.5W-12Al	67.3	15.9	5.0	11.9

Table 2 shows that the compositions of the alloys produced via arc melting and casting have slight deviations from the expected alloy compositions. The compositional deviation is due to the large variation in boiling points among the four constituent elements. The relatively low boiling point of Al leads to its sublimation, making it difficult for Al to fully and uniformly incorporate into the alloy. Among the samples, the actual composition of Nb-15Hf-5.5W-4Al was found to be Nb-15.1Hf-5.8W-3.5Al; this composition will be referred to as '4Al' in subsequent descriptions. The exact composition of Nb-15Hf-5.5W-8Al was Nb-17.5Hf-4.5W-7.6Al, which will be referred to as '8Al'. The exact composition of Nb-15Hf-5.5W-12Al was Nb-15.9Hf-5W-11.9Al, which will be referred to as '12Al' in the following sections.

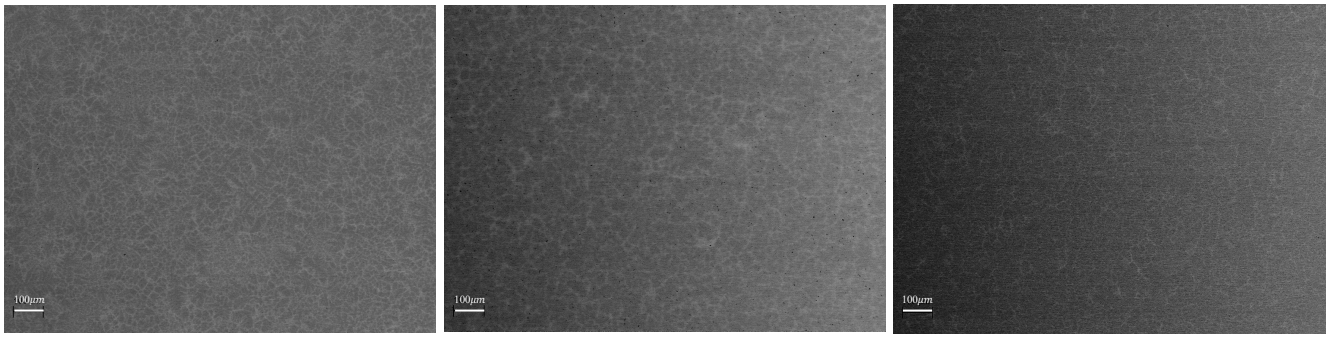

(a) *(b)* *(c)*

Figure 31. BSE images of three pre-oxidation samples (a) 4Al; (b) 8Al; (c)12Al

Figure 31 (a), (b), and (c) show SEM-BSE images of the three alloy compositions before oxidation. Their microstructures exhibit typical dendritic structures. EBSD (electron backscatter diffraction) results of three samples with different aluminum content (4Al, 8Al, 12Al) are shown in Figure 32. The false-color image shows the grain orientation distribution of different grains. The bar chart below shows the corresponding sample's equivalent circular diameters (i.e., grain sizes). It can be seen that the grain size of the sample gradually decreases with the increase of Al content (from 4Al to 12Al). The grain size of 12Al samples is smaller than that of 4Al and 8Al samples. This trend is also quantified in the bar chart below. The average grain size of the 4Al sample is the largest, reaching 44.52μm, while the average grain size of the 12Al sample is the smallest, 36.87μm. The bar chart further shows that the grain size distribution also changes with increased Al content. The grain size distribution of the 12Al sample is the most concentrated, which means that the grain size is more uniform. The grain size distribution of 4Al and 8Al samples is relatively

broad, especially the 4Al sample, showing a larger grain size distribution range. The increase in Al content leads to grain refinement, which may be because the increasing Al content limits the growth kinetics of the grains thus forming a finer grain structure. In addition, a reduction in grain size contributes to an increase in the material's yield stress, which is also consistent with the trend observed in hardness test results which come later in this chapter.

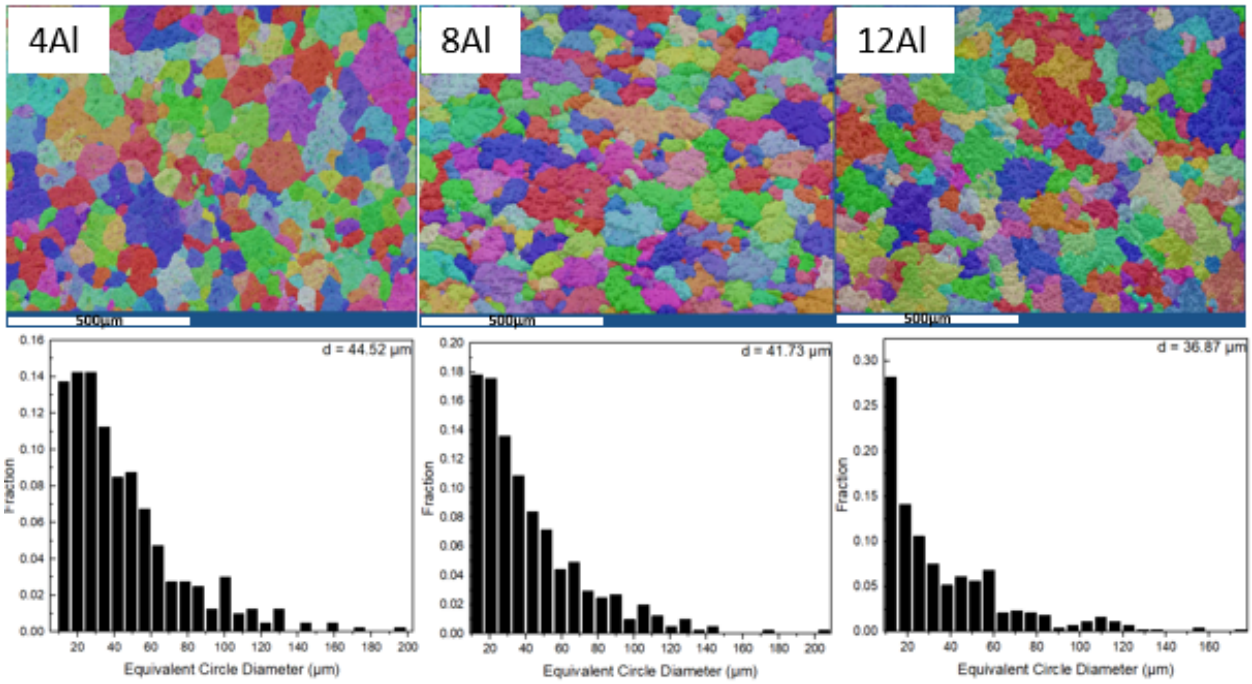

Figure 32. EBSD results of three pre-oxidation samples

Figure 33 represents the EDS mapping results for the 8Al sample before oxidation. The elemental distribution from the EDS results of the other two samples is similar (not shown for simplicity). The distribution of elements shows segregation in the dendritic structure: Hf(green) and Al(yellow) are mainly distributed in the inter-dendrite region. In contrast, W(orange) and matrix element Nb(red) are mainly distributed in the dendritic region. The segregation of Hf and Al in the inter-dendrite structure may affect the alloy's mechanical properties and oxidation behavior since Hf enhances toughness and Al is usually associated with forming a protective oxide layer.

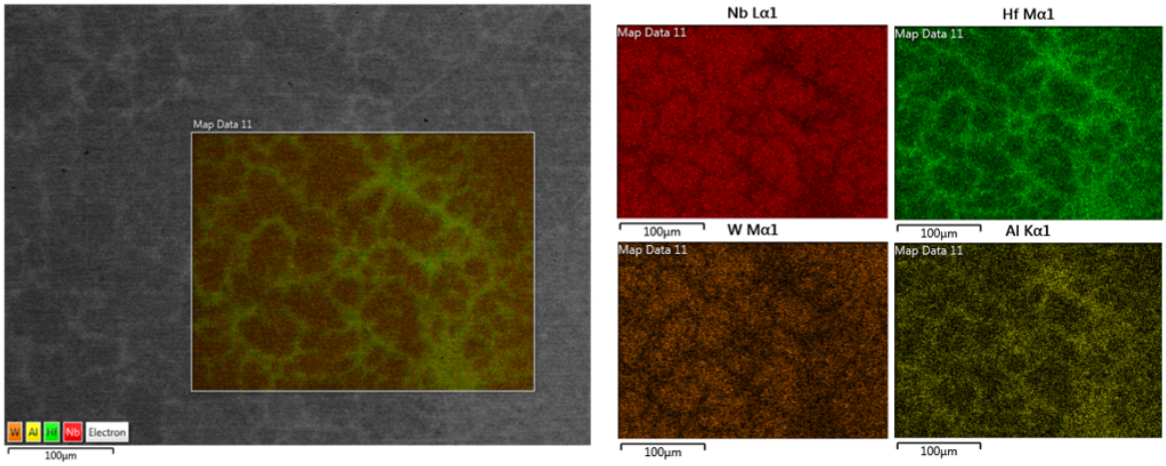

Figure 33. Elemental mapping of Nb-15Hf-5.5W-8Al

The X-ray diffraction study identified that all alloys before oxidation had a mainly single-phase bcc crystal structure. With the aluminum content increasing to 12 at%, a small peak corresponding to ordered B2 phase appeared. The XRD patterns in Figure 34 show that the peaks for the 8Al and 12Al samples gradually shift to the right, indicating a reduction in lattice parameters as the Al content increases.

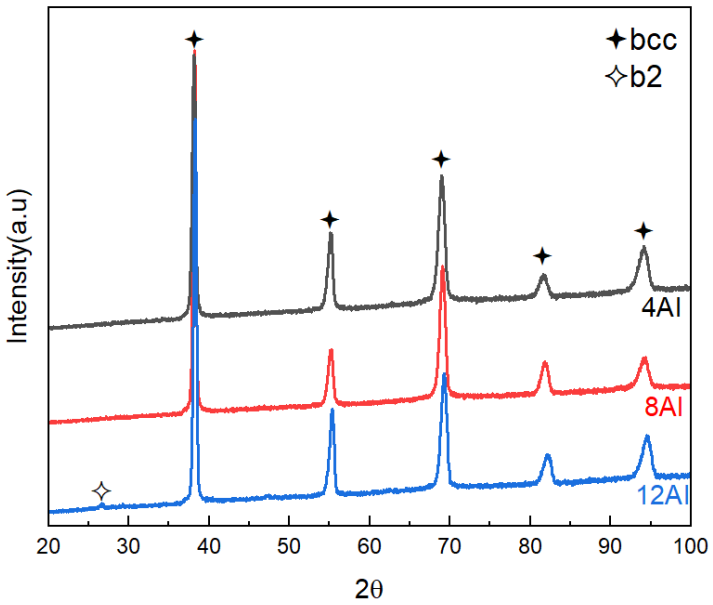

Figure 34. XRD pattern of three pre-oxidation samples

Table 3. Hardness of pre-oxidation samples

Alloys	Nb-15Hf-5.5W-4Al	Nb-15Hf-5.5W-8Al	Nb-15Hf-5.5W-12Al
Hardness	317±5 HV5	357±6 HV5	423±11 HV5

Table 3 presents the hardness of the three samples before oxidation. The hardness results are expressed in the form of the mean ± standard deviation. Using the data from this table, Figure 35 was generated. It shows that as the Al content increases, both the average hardness and the standard deviation gradually increase. The hardness increase is monotonic with the increasing Al content: the 4Al sample has the lowest hardness at 317±5 HV5, the 8Al sample has a medium hardness of 357±6 HV5, and the 12Al sample has the highest hardness at 423±11 HV5.

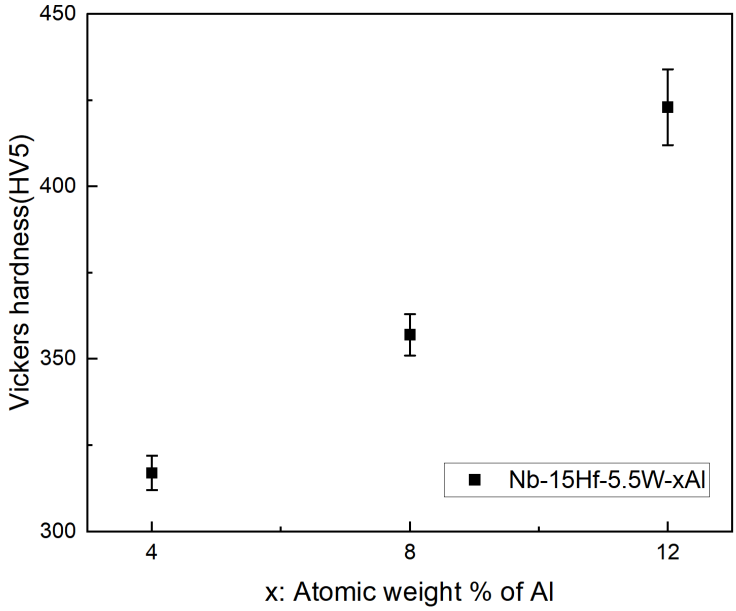

Figure 35. Hardness distribution of different Al content samples

As said, from 4Al to 12Al, the Vickers hardness increases monotonously. Figure 36 shows that high-density slip bands around indentations in 4Al and 8Al, indicative of plastic deformation; the 12Al sample showed cracks around the indentation, suggesting that an increase in hardness led to a decrease in ductility/toughness.

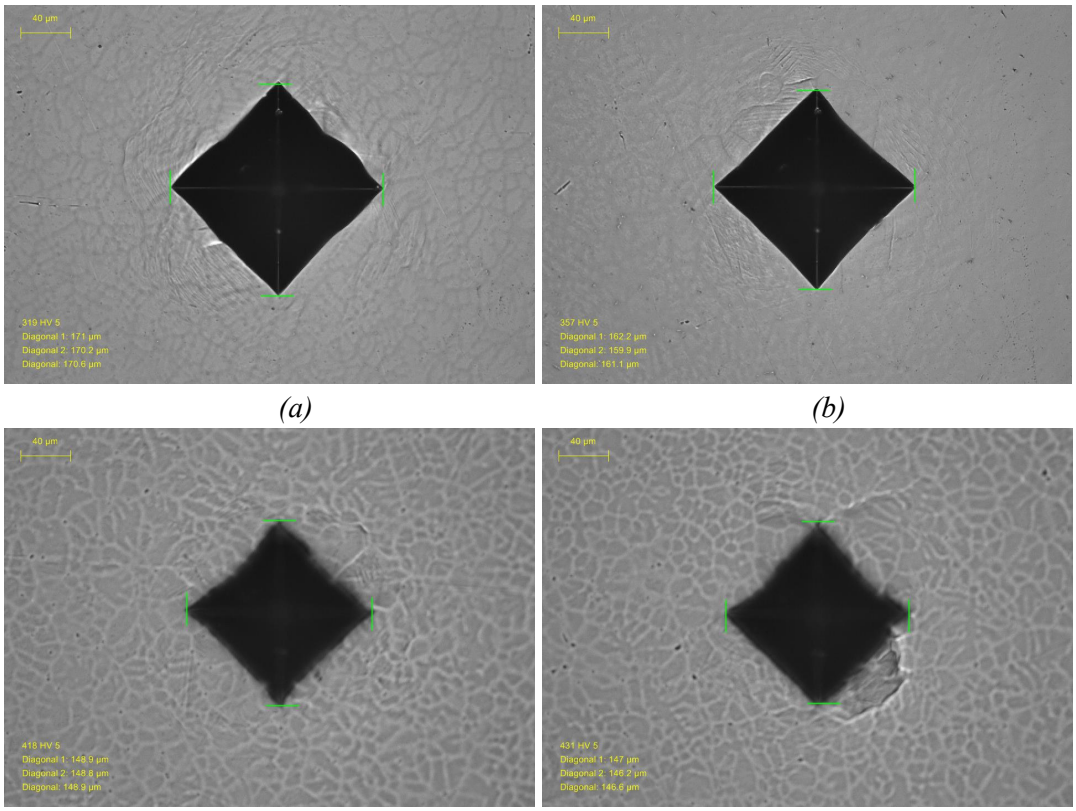

(a) *(b)*

(c) *(d)*

Figure 36. Indentation imprints from three samples (a) 4Al; (b) 8Al; (c) and (d)12Al

In summary, the experimental results of all pre-oxidation samples showed that the Al content greatly affected the microstructure and mechanical properties of the alloy. With the increase in Al content, the grain size of the sample decreased gradually, showing a finer and more uniform grain structure. At the same time, the increase in Al content led to the gradual increase of sample hardness, which was consistent with the trend of grain refinement. These results provided a basic understanding of the effect of Al on the microstructure and material properties of Nb-based refractory alloys.

6.2 Post-oxidation

The pictures in Table 4 below show how the oxidized samples looked after they were removed from the furnace where the oxidation studies were done. It can be observed that except for the three samples oxidized at 800℃ for 1 hour, which had no obvious pesting phenomenon, all the other samples showed pesting to different degrees. For samples oxidized at 800℃ for 8 hours and 24 hours, the pesting products presented a fine black powder. In contrast, for samples oxidized at 1000℃ and 1200℃, the pesting product appeared primarily black and yellow, requiring some grinding work to turn into powder. Two trends were obvious even before the oxidation kinetics analysis. First, the volume of spalled-off materials increased significantly with the increase of oxidation time. Second, with the increase of Al content, the volume of the spalled-off materials decreased obviously.

Table 4. The appearance of samples after oxidation tests. The crucible size: 20mm*20mm

Temperature ℃	800℃			1000℃			1200℃		
Time h	1h	8h	24h	1h	8h	24h	1h	8h	24h
4Al	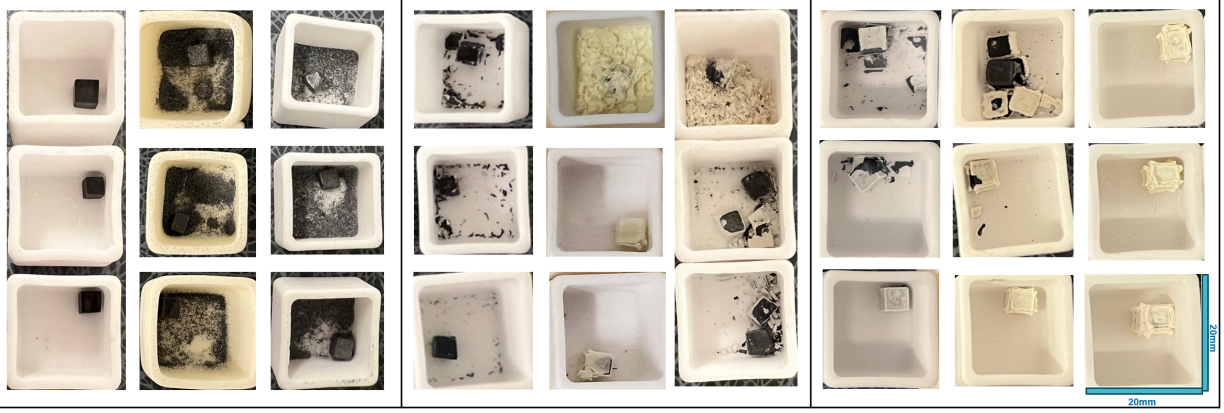								
8Al									
12Al									

6.2.1 Oxidation kinetics

The three diagrams in Figure 37 show the oxidation kinetics curves of samples with different Al contents (4Al, 8Al, 12Al) at 800℃, 1000℃, and 1200℃. The oxidation kinetics analysis was also quantified, following the growth rate law below:

The y-axis represents the mass gain of the sample per unit area (mg/cm²), and the x-axis represents the oxidation time (hours). The curve shows the oxidation behavior of samples with different Al contents over time at different temperatures.

$$\Delta m = kt^n$$

where Δm is the specific mass change normalized by the initial surface area (mg/cm²), k is the rate constant, t is the oxidation time, n is the time exponent, and R^2 indicates the quality of the fitting. Fitting results are summarized in Table 5.

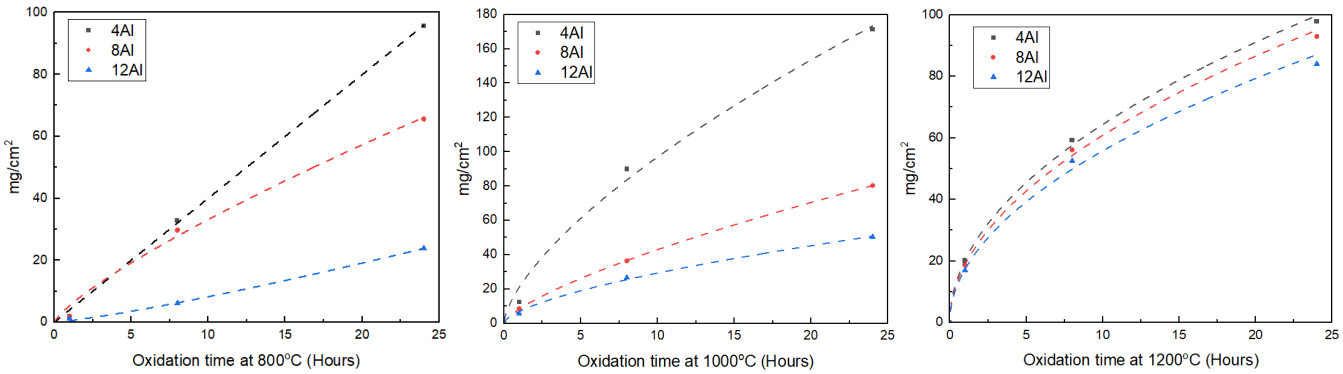

Figure 37. Oxidation kinetics curves of Nb-15Hf-5.5W-xAl (x=4, 8, 12) alloys with varying Al contents at 800°C, 1000°C, and 1200°C

At all three temperatures, it can be observed that the largest mass gain was in the 4Al sample, and the smallest mass gain was in the 12Al sample. This indicates that the increase in Al contents improved the oxidation resistance of the samples. The 12Al sample had the lowest oxidation rate at all temperatures and exhibited the best oxidation resistance.

The curve of 800°C shows an oxidation behavior close to a linear law ($n \approx 1$). As such, the oxidation process was controlled by the interface reaction, and the oxygen reacted directly with the sample surface to form an oxide layer, but this layer was thin and did not significantly hinder further oxidation. According to the pictures of oxidized samples shown above, there was an obvious pesting phenomenon on the samples at 800°C for 8h and 24h, and the oxidized products were presented as black powders. It can be inferred that at this temperature, the formation of oxides could not effectively block the diffusion of oxygen.

The oxidation curve at 1000°C begins to show a seemingly parabolic law trend ($n<1$), i.e., the oxidation rate gradually slowed down over time. This was due to the gradual thickening of the oxide layer, which hindered the penetration of oxygen and other diffusers (e.g., nitrogen), and the oxidation process began to be dominated by diffusion control. It can be seen from the sample pictures after oxidation that the pesting product of the sample at 1000°C contained black powders and yellow flakes. The occurrence of oxides spalling off after oxidation indicated that the oxide layer was thick but brittle, and it was easy to peel off.

The oxidation curve at 1200°C follows the parabolic law and has smaller n values than that at 1000 °C. At relatively high temperatures, the initial oxidation was fast, generating a large amount of oxidation products.

With the extension of time, the oxide layer rapidly became thicker, which slowed down further oxidation reactions, resulting in a decrease in the oxidation rate. Oxidation products of the sample appeared as a large amount of black and yellow flake-shaped materials, which needed to be ground to become powders. Compared to 1000 ℃, the oxide layer formed at such high temperatures was thicker and also more difficult to peel off.

The results of these oxidation kinetics curves clearly show that the Al content played a key role in improving the oxidation resistance of Nb-based refractory alloys. The samples with high Al contents had better oxidation resistance at all temperatures. These results provided an important basis for understanding the role of the Al content in Nb-based refractory alloys and their oxidation behavior at high temperatures. The oxidation kinetics can be classified according to the value of the time exponent n. As mentioned in the previous sub-chapter section 3.2.3, when n<1, the plot appears "parabolic," which means that the diffusion process mainly controls the oxidation rate. When n=1, the oxidation kinetics is said to be "linear," where the oxidation rate is limited by the reaction occurring at the oxide-metal interface.

Table 5. The oxidation coefficient (k) and the oxidation time exponent (n) of fitted growth rate law equations and the coefficient of determination (R^2)

Alloy	**k[mg cm^{-2}h^{-n}]**	**n**	**R^2**
T=800℃			
Nb-15Hf-5.5W-4Al	4.02954 ± 0.77093 (4.02786 ± 0.07409)	0.99732 ± 0.06206 (1)	0.99893 (0.99932)
Nb-15Hf-5.5W-8Al	5.39845 ± 2.00556 (2.7444 ± 0.26052)	0.78851 ± 0.12261 (1)	0.9922 (0.9823)
Nb-15Hf-5.5W-12Al	0.50489 ± 0.16471 (0.99211 ± 0.06091)	1.21309 ± 0.10464 (1)	0.99819 (0.99252)
T=1000℃			
Nb-15Hf-5.5W-4Al	21.0124 ± 6.67449	0.664 ± 0.10645	0.99043
Nb-15Hf-5.5W-8Al	8.26976 ± 0.2057	0.7152 ± 0.00828	0.99995
Nb-15Hf-5.5W-12Al	6.9234 ± 1.19043	0.62662 ± 0.05795	0.99654
T=1200℃			
Nb-15Hf-5.5W-4Al	20.33254 ± 1.90497	0.50034 ± 0.03234	0.99779
Nb-15Hf-5.5W-8Al	18.81035 ± 2.00637	0.50959 ± 0.03674	0.99727
Nb-15Hf-5.5W-12Al	17.31119 ± 3.00646	0.50808 ± 0.05984	0.99249

The data in Table 5 shows the oxidation coefficient k, oxidation exponent n, and the coefficient of determination R^2 for three different alloys with varying Al contents, tested under different temperatures with different durations of time. For the 800℃ data, the oxidation kinetics appears linear, i.e., n is close to 1. To reflect the seen oxidation behavior more reasonably, n was fixed to 1 and the oxidation coefficient k, and the coefficient of determination R^2 were recalculated. The newly obtained fitting results are shown in brackets in Table 5. For 1000℃ and 1200℃, the value of n is less than 1, which is consistent with the previous analysis of oxidation kinetics curves. The fitting results show that the oxidation process is mainly parabolic, especially at 1200℃. As the temperature increases, the rate of oxidation decreases (n decreases) because an oxide layer forms that prevents the rapid diffusion of oxygen inward. The switch from linear to parabolic kinetics corresponds to the change in the oxidation reaction mechanism under different conditions.

6.2.2 Microstructure and phase constitution of oxidation products

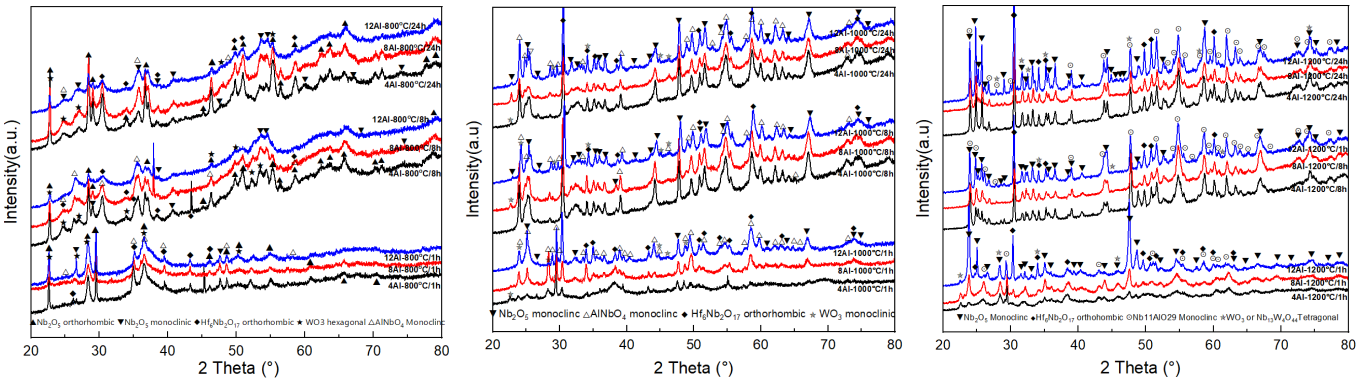

(a) (b) (c)

Figure 38. XRD patterns samples after oxidation at (a) 800℃ (b) 1000℃ (c) 1200℃

Table 6. XRD results summary

Temperature/℃	800℃			1000℃			1200℃		
Time/h	1h (bulk surface)	8h (powders)	24h (powders)	1h (bulk surface)	8h (powders)	24h (powders)	1h (bulk surface)	8h (powders)	24h (powders)
4Al, 8Al, 12Al	Nb_2O_5 (orthorhombic) Nb_2O_5 (monoclinic, trace amount) $Hf_6Nb_2O_{17}$ (orthorhombic) $AlNbO_4$ (monoclinic) WO_3 (hexagonal)			$AlNbO_4$ (monoclinic) Nb_2O_5 (monoclinic) $Hf_6Nb_2O_{17}$ (orthorhombic) WO_3 (monoclinic)			Nb_2O_5 (monoclinic) $Hf_6Nb_2O_{17}$ (orthorhombic) $Nb_{11}AlO_{29}$ (monoclinic) WO_3 (tetragonal, monoclinic) $Nb_{13}W_4O_{44}$ (monoclinic, 24h)		

XRD analysis of oxidized samples shows a variety of phases, as shown in Figure 38 and Table 6. Figures 38 (a), (b), and (c) present the XRD pattern of all samples at three temperatures. It can be seen that the types of oxidation products of samples with different compositions at different times are almost the same at the same temperature, although their contents are different. Oxidation at different temperatures also led to different crystal structures of the same oxide (for example Nb_2O_5 and WO_3), which are shown in detail in Table 6. Recalling the discussion on complex protective scales in the previous chapter, the oxidation products here are all complex.

At 800℃, for the 1h oxidized sample, the main phases detected were Nb_2O_5 (orthorhombic) and $Hf_6Nb_2O_{17}$ (orthorhombic). In addition, a trace amount of monoclinic Nb_2O_5 and hexagonal WO_3 was also found in the sample. After 8h and 24h of oxidation, the monoclinic Nb_2O_5 phase increased in the sample and the monoclinic $AlNbO_4$ phase was also detected.

At 1000℃, the 1h oxidized sample mainly consisted of the $AlNbO_4$ (monoclinic) and $Hf_6Nb_2O_{17}$ (orthorhombic) phases. The monoclinic phase of Nb_2O_5 dominated over the orthorhombic one and its content increased with time in the 8h and 24h oxidized samples, and the monoclinic WO_3 appeared. These results show that the crystal structure of oxidation products evolved with increasing temperature, indicating that the crystal structure of oxides changed at different temperatures.

At 1200℃, Nb_2O_5 (monoclinic) and $Hf_6Nb_2O_{17}$ (orthorhombic) phases remained in the 1h oxidized sample, and new phases $Nb_{11}AlO_{29}$ (monoclinic) and WO_3 (tetragonal) appeared. Here, tetragonal phase of WO_3 usually appears as the product of low-temperature oxidation, but after high-temperature oxidation, the sample may change from high-temperature to low-temperature phases (such as monoclinic and tetragonal phases) during cooling. In this process, if the cooling rate is fast or the local temperature gradient is present, some phases may be preserved and even mixed phases may be produced. In the 24h oxidized sample, a $Nb_{13}W_4O_{44}$ (monoclinic) phase was detected, indicating that the oxidation products at high temperatures were more complex, and the mixture of tetragonal and monoclinic phases of tungsten-related oxides was further formed with the increase of oxidation time.

From the seen oxidation products at different oxidation temperatures, it was found that increasing temperature resulted in the emergence of some new phases that were difficult to form at low temperatures, and phase transitions of some existing phases (e.g., orthorhombic Nb_2O_5 to monoclinic Nb_2O_5). In particular, the formation of $AlNbO_4$ and $Nb_{11}AlO_{29}$ phases was more obvious in the samples with higher Al contents, indicating that the addition of Al played an important role in forming different Al-containing complex oxides, potentially contributing to slow down the high-temperature oxidation process.

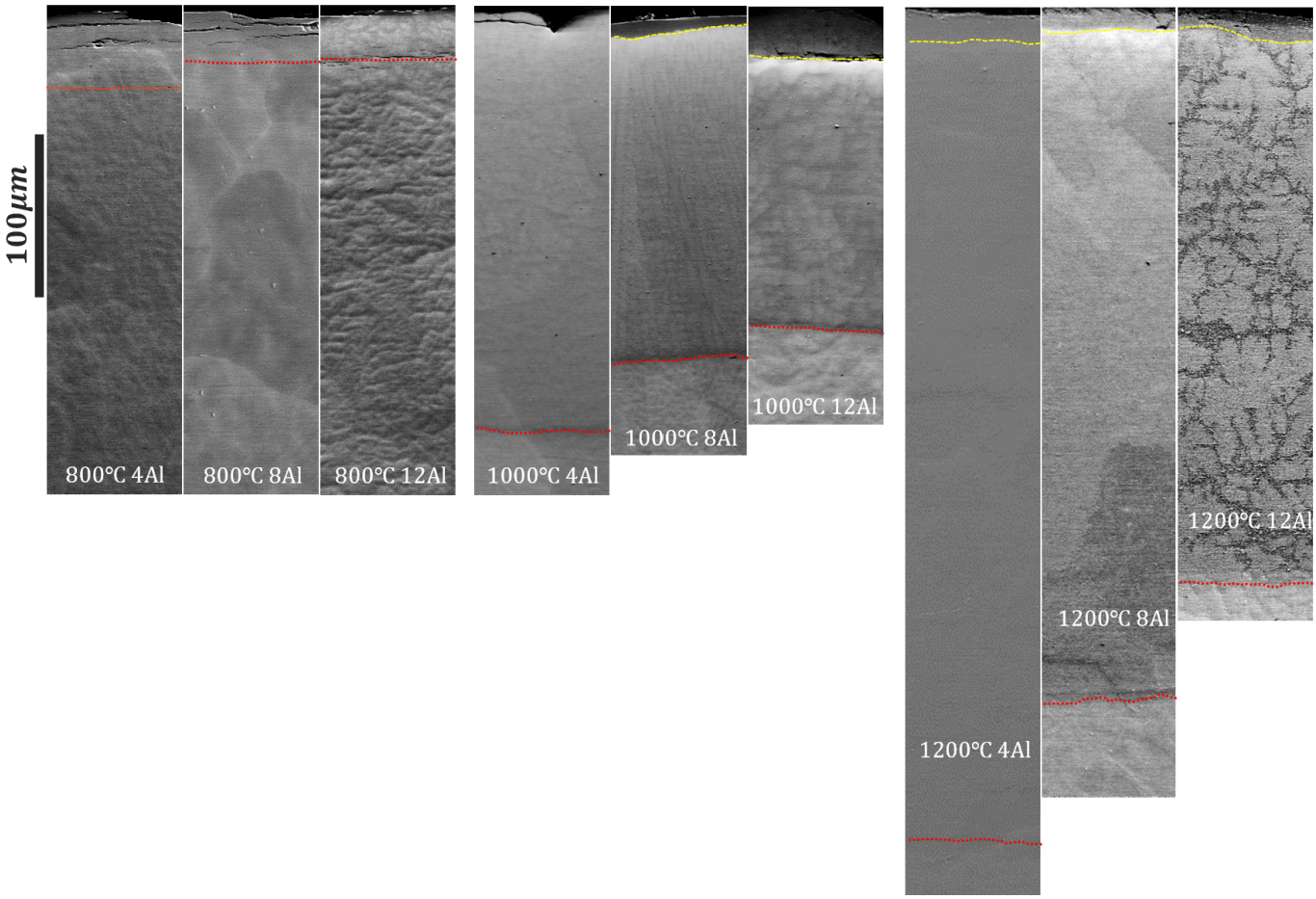

Figure 39. The oxide layer and transition layer on the edge of the cross-section of all 8h oxidized samples.

SEM images in Figure 39 show cross-sectional observations of all samples after 8h of oxidation at three temperatures with different Al contents. At 800℃, no distinction between the oxide layer and the transition layer was observed in all samples, indicating that the oxidation process was a direct reaction between alloys

and oxygen corresponding to interface-controlled diffusion leading to linear oxidation. At 1000℃, the 4Al sample also showed no obvious distinction between the oxide layer and the transition layer, while the 8Al and 12Al samples showed a clear distinction between the two. For the 4Al sample, as seen from Table 4 on the appearance indicating obvious pesting, it can be inferred that the oxide layer was almost completely spalled off. The higher Al content helped to enhance the oxide layer adhesion to the material underneath, and therefore some oxide layer remained to be seen on top of the transition later in the 8Al and 12Al samples.

Table 7. The thickness of the oxide layer (t_oxide) and the transition layer (t_tranistion), measured for 8h oxidized samples from Figure 39

Temperature	**t_oxide**	**t_transition**	**t_oxide**	**t_transition**	**t_oxide**	**t_transition**
	4Al		8Al		12Al	
800 ℃	-	45μm	-	27μm	-	25μm
1000 ℃	-	250μm	12μm	186μm	30μm	118μm
1200 ℃	20μm	470μm	13μm	397μm	15μm	309μm

At 1200℃, all the samples showed a clear distinction between the oxide and the transition layer. It can be observed that the thickness of the transition layer increased with the increase of temperature and the decrease of Al content (Table 7). Less could be concluded regarding the thickness of the oxide layer though, due to their spalling off. Therefore, it appeared that adding Al up to 12 at% helped to improve the oxidation resistance; it was however not sufficient to form a dense and protective oxide layer, e.g., the expected Al_2O_3 layer or a complex oxide layer that is sufficiently protective.

7 Conclusions

1. Microstructures of three alloys, Nb-15Hf-5.5W-4Al, Nb-15Hf-5.5W-8Al, and Nb-15Hf-5.5W-12Al (at.%), all showed a single-phase bcc structure with typical dendritic structure, where Nb and W were enriched in dendrite regions and Hf and Al were enriched in inter-dendritic regions. Grain size refinement was observed with the increase of Al content. The ordering of the bcc crystal structure was seen in the 12Al sample. Vicker hardness monotonously increased with the increasing Al content.
2. Different degrees of pesting were observed in almost all samples, except the condition for oxidation at 800℃ for 1h. Pesting became more significant at higher temperatures with longer oxidation times. The increase of Al content up to 12 at% reduced the severity of pesting, which was however not fully suppressed.
3. The oxidation behavior of the alloys experienced a transition from linear mode at 800℃, to semi-parabolic at 1000℃, and to parabolic at 1200℃. At 800 ℃, the interfacial reaction controlled the oxidation process, while the oxidation was controlled by the diffusion mechanism at 1000℃ and 1200℃.
4. Different complex oxide phases were produced at different temperatures, including orthorhombic $Hf_6Nb_2O_{17}$, monoclinic $AlNbO_4$, and monoclinic $Nb_{11}AlO_{29}$. The crystal structure of oxides transformed with increasing temperature, e.g., from orthorhombic Nb_2O_5 to monoclinic Nb_2O_5, and from hexagonal WO_3 to monoclinic and tetragonal WO_3. Meanwhile, the change of oxides was also observed at different temperatures, e.g., from monoclinic $AlNbO_4$ at 800℃ and 1000℃ to monoclinic $Nb_{11}AlO_{29}$ at 1200℃.
5. At 1000℃ (except 4Al) and 1200℃, the 8h oxidized samples exhibited a clear distinction between the oxide layer and the transition layer. The thickness of the transition layer increased with the increase of temperature and the decrease of Al content. Adding Al up to 12 at% did help to improve the oxidation resistance, but it was not sufficient to form a dense and protective layer.

References

[1] J. H. Perepezko, “The Hotter the Engine, the Better,” *Science*, vol. 326, pp. 1068–1069, Nov. 2009, doi: 10.1126/science.1179327.

[2] Z. Huda, T. Zaharinie, and H. A. Al-Ansary, “Enhancing power output and profitability through energy-efficiency techniques and advanced materials in today’s industrial gas turbines,” Dec. 01, 2014, *Springer*. doi: 10.1186/s40712-014-0002-y.

[3] . Nageswara Rao Muktinutalapati, *Materials for Gas Turbines - An Overview*. INTECH Open Access Publisher, 2011.

[4] O. N. Senkov, G. B. Wilks, D. B. Miracle, C. P. Chuang, and P. K. Liaw, “Refractory high-entropy alloys,” *Intermetallics (Barking)*, vol. 18, no. 9, pp. 1758–1765, 2010.

[5] Y. Zhang *et al.*, “Microstructures and properties of high-entropy alloys,” *Prog Mater Sci*, vol. 61, pp. 1–93, 2014, doi: https://doi.org/10.1016/j.pmatsci.2013.10.001.

[6] T.-K. Tsao *et al.*, “The High Temperature Tensile and Creep Behaviors of High Entropy Superalloy,” *Sci Rep*, vol. 7, no. 1, p. 12658, 2017, doi: 10.1038/s41598-017-13026-7.

[7] M. P. Brady, B. Gleeson, and I. G. Wright, “Alloy Design Strategies for Promoting Protective Oxide-Scale Formation,” 2000.

[8] C.-H. Chang, M. S. Titus, and J.-W. Yeh, “Oxidation Behavior between 700 and 1300 °C of Refractory TiZrNbHfTa High-Entropy Alloys Containing Aluminum,” *Adv Eng Mater*, vol. 20, no. 6, p. 1700948, Jun. 2018, doi: https://doi.org/10.1002/adem.201700948.

[9] G. B. Viswanathan, Z. T. Kloenne, J.-P. Couzinié, B. A. Welk, S. J. Kuhr, and H. L. Fraser, “Deformation mechanisms and their role in the lack of ductility in the refractory-based high entropy alloy AlMo0.5NbTa0.5TiZr,” *Acta Mater*, vol. 269, p. 119824, 2024, doi: https://doi.org/10.1016/j.actamat.2024.119824.

[10] V. V Satya Prasad, R. G. Baligidad, and A. A. Gokhale, “Niobium and Other High Temperature Refractory Metals for Aerospace Applications,” in *Aerospace Materials and Material Technologies : Volume 1: Aerospace Materials*, N. E. Prasad and R. J. H. Wanhill, Eds., Singapore: Springer Singapore, 2017, pp. 267–288. doi: 10.1007/978-981-10-2134-3_12.

[11] O. N. Senkov, S. Gorsse, D. B. Miracle, S. I. Rao, and T. M. Butler, “Correlations to improve high-temperature strength and room temperature ductility of refractory complex concentrated alloys,” *Mater Des*, vol. 239, p. 112762, 2024, doi: https://doi.org/10.1016/j.matdes.2024.112762.

[12] M. S. El-Genk and J. M. Tournier, “A review of refractory metal alloys and mechanically alloyed-oxide dispersion strengthened steels for space nuclear power systems,” Apr. 01, 2005. doi: 10.1016/j.jnucmat.2004.10.118.

[13] I. Razumovskii, B. Bokstein, and M. Razumovsky, “Approaches to the Development of Advanced Alloys Based on Refractory Metals,” *Encyclopedia*, vol. 3, no. 1, pp. 311–326, Mar. 2023, doi: 10.3390/encyclopedia3010019.

[14] M. Krüger, O. Kauss, K. Naumenko, C. Burmeister, E. Wessel, and J. Schmelzer, “The potential of mechanical alloying to improve the strength and ductility of Mo–9Si–8B–1Zr alloys – experiments and simulation,” *Intermetallics (Barking)*, vol. 113, p. 106558, 2019, doi: https://doi.org/10.1016/j.intermet.2019.106558.

[15] D. B. Miracle and O. N. Senkov, “A critical review of high entropy alloys and related concepts,” Jan. 01, 2017, *Elsevier Ltd*. doi: 10.1016/j.actamat.2016.08.081.

[16] J. W. Yeh *et al.*, “Nanostructured high-entropy alloys with multiple principal elements: Novel alloy design concepts and outcomes,” *Adv Eng Mater*, vol. 6, no. 5, pp. 299–303, 2004, doi: 10.1002/adem.200300567.
[17] B. Cantor, I. T. H. Chang, P. Knight, and A. J. B. Vincent, “Microstructural development in equiatomic multicomponent alloys,” *Materials Science and Engineering: A*, vol. 375–377, no. 1-2 SPEC. ISS., pp. 213–218, Jul. 2004, doi: 10.1016/j.msea.2003.10.257.
[18] J. Yeh, S. Chen, J. Gan, and S. Lin, “Communications: Formation of Simple Crystal Structures in Cu-Co-Ni-Cr-Al-Fe-Ti-V Alloys with Multiprincipal Metallic Elements,” 2004.
[19] J. W. Yeh, “Recent progress in high-entropy alloys,” *Annales de Chimie: Science des Materiaux*, vol. 31, no. 6, pp. 633–648, Nov. 2006, doi: 10.3166/acsm.31.633-648.
[20] S. Guo, Q. Hu, C. Ng, and C. T. Liu, “More than entropy in high-entropy alloys: Forming solid solutions or amorphous phase,” *Intermetallics (Barking)*, vol. 41, pp. 96–103, 2013, doi: https://doi.org/10.1016/j.intermet.2013.05.002.
[21] O. N. Senkov, D. B. Miracle, K. J. Chaput, and J.-P. Couzinie, “Development and exploration of refractory high entropy alloys—A review,” *J Mater Res*, vol. 33, no. 19, pp. 3092–3128, 2018.
[22] B. Chen and L. Zhuo, “Latest progress on refractory high entropy alloys: Composition, fabrication, post processing, performance, simulation and prospect,” *Int J Refract Metals Hard Mater*, vol. 110, p. 105993, 2023.
[23] L. Lilensten, J. P. Couzinié, L. Perrière, J. Bourgon, N. Emery, and I. Guillot, “New structure in refractory high-entropy alloys,” *Mater Lett*, vol. 132, pp. 123–125, 2014, doi: https://doi.org/10.1016/j.matlet.2014.06.064.
[24] J. Zhou, Y. Cheng, Y. Chen, and X. Liang, “Composition design and preparation process of refractory high-entropy alloys: A review,” *Int J Refract Metals Hard Mater*, vol. 105, p. 105836, 2022, doi: https://doi.org/10.1016/j.ijrmhm.2022.105836.
[25] W. Chen, Q. H. Tang, H. Wang, Y. C. Xie, X. H. Yan, and P. Q. Dai, “Microstructure and mechanical properties of a novel refractory AlNbTiZr high-entropy alloy,” *Materials Science and Technology*, vol. 34, no. 11, pp. 1309–1315, Jul. 2018, doi: 10.1080/02670836.2018.1446267.
[26] M. Srikanth, A. Raja Annamalai, A. Muthuchamy, and C. P. Jen, “A review of the latest developments in the field of refractory high-entropy alloys,” Jun. 01, 2021, *MDPI AG*. doi: 10.3390/cryst11060612.
[27] M. A. Tunes, H. T. Vo, J. K. S. Baldwin, T. A. Saleh, S. J. Fensin, and O. El-Atwani, “Perspectives on novel refractory amorphous high-entropy alloys in extreme environments,” *Appl Mater Today*, vol. 32, p. 101796, 2023, doi: https://doi.org/10.1016/j.apmt.2023.101796.
[28] S. Maiti and W. Steurer, “Structure and Properties of Refractory High-Entropy Alloys,” in *TMS 2014: 143rd Annual Meeting & Exhibition*, Cham: Springer International Publishing, 2016, pp. 1093–1096.
[29] M. C. Gao, C. S. Carney, Ö. N. Doğan, P. D. Jablonksi, J. A. Hawk, and D. E. Alman, “Design of Refractory High-Entropy Alloys,” *JOM*, vol. 67, no. 11, pp. 2653–2669, 2015, doi: 10.1007/s11837-015-1617-z.
[30] Z. Wang *et al.*, “Solving oxygen embrittlement of refractory high-entropy alloy via grain boundary engineering,” *Materials Today*, vol. 54, pp. 83–89, 2022.
[31] Y. Cui *et al.*, “Interstitially carbon-alloyed refractory high-entropy alloys with a body-centered cubic structure,” *Sci China Mater*, vol. 65, no. 2, pp. 494–500, 2022.
[32] X. Shen *et al.*, “Intermediate-temperature creep behaviors of an equiatomic VNbMoTaW refractory high-entropy alloy,” *Journal of Materials Research and Technology*, vol. 24, pp. 4796–4807, 2023, doi: https://doi.org/10.1016/j.jmrt.2023.04.141.
[33] J.-Ph. Couzinié, L. Lilensten, Y. Champion, G. Dirras, L. Perrière, and I. Guillot, “On the room temperature deformation mechanisms of a TiZrHfNbTa refractory high-entropy alloy,” *Materials Science and Engineering: A*, vol. 645, pp. 255–263, 2015, doi: https://doi.org/10.1016/j.msea.2015.08.024.

[34] J. Zhang *et al.*, “Zr diffusion in BCC refractory high entropy alloys: A case of ’non-sluggish’ diffusion behavior,” *Acta Mater*, vol. 233, p. 117970, Apr. 2022, doi: 10.1016/j.actamat.2022.117970.
[35] “Introduction to the High-Temperature Oxidation of Metals”.
[36] D. R. Gaskell and D. E. Laughlin, *Introduction to the Thermodynamics of Materials*. CRC press, 2017.
[37] G. Franceschin, N. de J. Flores Martinez, G. Vázquez.Victorio, S. Merah, and R. Valenzuela, “Sintering and Reactive Sintering by Spark Plasma Sintering (SPS),” 2018. doi: 10.5772/intechopen.68871.
[38] C. Xu and W. Gao, “Pilling-bedworth ratio for oxidation of alloys,” *Materials Research Innovations*, vol. 3, no. 4, pp. 231–235, 2000, doi: 10.1007/s100190050008.
[39] C. Wagner, “Z. fuḶr Elektrochem,” *Ber. Bunsenges. Phys. Chem*, vol. 63, pp. 772–782, 1959.
[40] W. D. Klopp, D. J. Maykuth, C. T. Sims, and R. I. Jaffee, “OXIDATION AND CONTAMINATION REACTIONS OF NIOBIUM AND NIOBIUM ALLOYS,” 1959.
[41] J. D. James, J. A. Spittle, S. G. R. Brown, and R. W. Evans, “A review of measurement techniques for the thermal expansion coefficient of metals and alloys at elevated temperatures,” 2001. [Online]. Available: www.iop.org/Journals/mt
[42] W. Knabl, G. Leichtfried, and R. Stickler, “Refractory Metals and Refractory Metal Alloys,” in *Springer Handbook of Materials Data*, H. Warlimont and W. Martienssen, Eds., Cham: Springer International Publishing, 2018, pp. 307–337. doi: 10.1007/978-3-319-69743-7_13.
[43] H. A. Miley, “Theory of oxidation and tarnishing of metals: I. The linear, parabolic and logarithmic laws,” *Transactions of The Electrochemical Society*, vol. 81, no. 1, p. 391, 1942.
[44] A. Ali, “Comparative Study on High Temperature Oxidation Behavior of Austenitic Stainless Steels in Different Environments”, doi: 10.13140/RG.2.1.2677.9042.
[45] J. W. X. Wo, M. C. Hardy, and H. J. Stone, “Evaluating Wagner Oxidation Criteria for Protective Al2O3 Scale Formation in Ni-Based Superalloys,” *High Temperature Corrosion of Materials*, vol. 100, no. 1–2, pp. 85–108, Aug. 2023, doi: 10.1007/s11085-023-10163-5.
[46] T. Ohmi, Y. Nakagawa, M. Nakamura, A. Ohki, and T. Koyama, “Formation of chromium oxide on 316L austenitic stainless steel,” *Journal of Vacuum Science & Technology A: Vacuum, Surfaces, and Films*, vol. 14, no. 4, pp. 2505–2510, Jul. 1996, doi: 10.1116/1.580010.
[47] M. Jepson and R. L. Higginson, “The use of EBSD to study the microstructural development of oxide scales on 316 stainless steel,” *Materials at High Temperatures*, vol. 22, no. 3–4, pp. 195–200, Jan. 2005, doi: 10.1179/mht.2005.022.
[48] Y. Lalau, S. Rigal, J.-P. Bedecarrats, and D. Haillot, “Latent Thermal Energy Storage System for Heat Recovery between 120 and 150 °C: Material Stability and Corrosion,” *Energies (Basel)*, vol. 17, p. 787, Feb. 2024, doi: 10.3390/en17040787.
[49] S. Burk, B. Gorr, V. B. Trindade, U. Krupp, and H.-J. Christ, “High temperature oxidation of mechanically alloyed Mo–Si–B alloys,” *Corrosion Engineering, Science and Technology*, vol. 44, no. 3, pp. 168–175, Jun. 2009, doi: 10.1179/174327809X419122.
[50] S. Sheikh, L. Gan, X. Montero, H. Murakami, and S. Guo, “Forming protective alumina scale for ductile refractory high-entropy alloys via aluminizing,” *Intermetallics (Barking)*, vol. 123, Aug. 2020, doi: 10.1016/j.intermet.2020.106838.
[51] H. Grabke J., M. Brumm W., M. Steinhorst, and B. Wagemann, “Accelerated oxidation of aluminides at intermediate temperatures,” *J. Phys. IV France*, vol. 03, no. C9, pp. C9-385-C9-393, Dec. 1993, [Online]. Available: https://doi.org/10.1051/jp4:1993940
[52] H. J. [Max-P.-I. fuer E. G. “Grabke Duesseldorf (Germany)]” *et al.*, “Intergranular oxidation and pesting of intermetallic compounds,” vol. 207–209, 1996, doi: https://doi.org/.
[53] “Pesting of the High. Temperature Intermetallic MoSi 2.”
[54] B. Gorr, M. Azim, H.-J. Christ, T. Mueller, D. Schliephake, and M. Heilmaier, “Phase equilibria, microstructure, and high temperature oxidation resistance of novel refractory high-entropy alloys,” *J Alloys Compd*, vol. 624, pp. 270–278, 2015.

[55] S. Becker, A. Rahmel, M. Schorr, and M. Schiitze, “Mechanism of Isothermal Oxidation of the Intermetallic TiAI and of TiA1 Alloys,” 1992.
[56] E. A. Anber *et al.*, “Oxidation resistance of Al-containing refractory high-entropy alloys,” *Scr Mater*, vol. 244, Apr. 2024, doi: 10.1016/j.scriptamat.2024.115997.
[57] S. Lu, X. Li, X. Liang, W. Shao, W. Yang, and J. Chen, “Effect of Al content on the oxidation behavior of refractory high-entropy alloy AlMo0.5NbTa0.5TiZr at elevated temperatures,” *Int J Refract Metals Hard Mater*, vol. 105, Jun. 2022, doi: 10.1016/j.ijrmhm.2022.105812.
[58] R. Zhang, J. Meng, J. Han, K. Tulugan, and R. Zhang, “Oxidation resistance properties of refractory high-entropy alloys with varied AlxCrTiMo content,” *J Mater Sci*, vol. 56, pp. 3551–3561, 2021.
[59] Y. Yan, K. A. McGarrity, D. J. Delia, C. Fekety, and K. Wang, “The oxidation-resistance mechanism of WTaNbTiAl refractory high entropy alloy,” *Corros Sci*, vol. 204, Aug. 2022, doi: 10.1016/j.corsci.2022.110377.
[60] T. M. Butler, K. J. Chaput, J. R. Dietrich, and O. N. Senkov, “High temperature oxidation behaviors of equimolar NbTiZrV and NbTiZrCr refractory complex concentrated alloys (RCCAs),” *J Alloys Compd*, vol. 729, pp. 1004–1019, 2017.
[61] S. Sheikh, L. Gan, A. Ikeda, H. Murakami, and S. Guo, “Alloying effect on the oxidation behavior of a ductile Al0.5Cr0.25Nb0.5Ta0.5Ti1.5 refractory high-entropy alloy,” *Mater Today Adv*, vol. 7, Sep. 2020, doi: 10.1016/j.mtadv.2020.100104.
[62] F. Müller *et al.*, “On the oxidation mechanism of refractory high entropy alloys,” *Corros Sci*, vol. 159, Oct. 2019, doi: 10.1016/j.corsci.2019.108161.
[63] B. J. Inkson, “Scanning electron microscopy (SEM) and transmission electron microscopy (TEM) for materials characterization,” in *Materials characterization using nondestructive evaluation (NDE) methods*, Elsevier, 2016, pp. 17–43.
[64] V.-D. Hodoroaba, “Energy-dispersive X-ray spectroscopy (EDS),” in *Characterization of Nanoparticles*, Elsevier, 2020, pp. 397–417.
[65] A. A. Bunaciu, E. G. UdriŞTioiu, and H. Y. Aboul-Enein, “X-ray diffraction: instrumentation and applications,” *Crit Rev Anal Chem*, vol. 45, no. 4, pp. 289–299, 2015.
[66] A. R. Franco Jr, G. Pintaúde, A. Sinatora, C. E. Pinedo, and A. P. Tschiptschin, “The use of a Vickers indenter in depth sensing indentation for measuring elastic modulus and Vickers hardness,” *Materials Research*, vol. 7, pp. 483–491, 2004.

DEPARTMENT OF INDUSTRIAL AND MATERIALS SCIENCE
CHALMERS UNIVERSITY OF TECHNOLOGY
Gothenburg, Sweden 2024
www.chalmers.se

CHALMERS
UNIVERSITY OF TECHNOLOGY